Research Square

Preprints are preliminary reports that have not undergone peer review.
They should not be considered conclusive, used to inform clinical practice,
or referenced by the media as validated information.

Phloroglucinol suppresses esophageal squamous cell carcinoma metastasis by modulating TGF-β/SMAD2/3/SNAI2 signaling and macrophage-derived paracrine TGF-β

CHAO WANG
Macau University of Science and Technology
Siji Nian
Southwest Medical University
Tao Xiong
Southwest Medical University
Xiaoke Sun
Southwest Medical University
Yingchun Ye
Southwest Medical University
Lin Li
Southwest Medical University
Qin Liu
Southwest Medical University
Wenfeng Xu
Southwest Medical University
Wenzhe Ma
Macau University of Science and Technology
Qing Yuan
qingyuan@swmu.edu.cn

Southwest Medical University

Article

Keywords: Phloroglucinol, Esophageal squamous cell carcinoma, Tumor-associated macrophages, Epithelial-mesenchymal transition, TGF-β/SMAD signaling, SNAI2 (Slug), Macrophage reprogramming, Metastasis

Posted Date: November 5th, 2026

DOI: https://doi.org/10.21203/rs.3.rs-11246931/v1

License: This work is licensed under a Creative Commons Attribution 4.0 International License.
Read Full License

Additional Declarations: No competing interests reported.

Phloroglucinol suppresses esophageal squamous cell carcinoma metastasis by modulating TGF-β/SMAD2/3/SNAI2 signaling and macrophage-derived paracrine TGF-β

Chao Wang [a,b,c,1], Siji Nian [b,1], Tao Xiong [b], Xiaoke Sun [b], Yingchun Ye [b], Lin Li [b], Qin Liu [b], Wenfeng Xu [b], Yongjian Li [b], Wenzhe Ma [a,*], Qing Yuan [a,b,*]

a. State Key Laboratory of Quality Research in Chinese Medicine & Faculty of Chinese Medicine, Macau University of Science and Technology, Macau, 999078, China

b. Public Center of Experimental Technology, The School of Basic Medical Sciences, Southwest Medical University, Luzhou, Sichuan province, 646000, China

c. Department of Thoracic Surgery, Affiliated Hospital of Southwest Medical University, Luzhou, Sichuan, 646000, China

[*] Corresponding authors:

Prof. Qing Yuan: qingyuan@swmu.edu.cn

Prof. Wen-Zhe Ma: wzma@must.edu.mo

[1] Contributed equally

Abstract

Esophageal squamous cell carcinoma (ESCC) is characterized by aggressive metastatic progression. Although Phloroglucinol (PhG), a clinically used natural polyphenolic compound, exhibits anti-tumor activity, whether it coordinately targets tumor cells and the tumor microenvironment during ESCC metastasis remains unclear.

The present study demonstrated that PhG significantly inhibited ESCC cell migration and invasion in vitro and suppressed tumor metastasis in zebrafish and mouse models. Transcriptomic profiling and functional validation revealed that PhG attenuated TGF-β-induced SMAD2/3 phosphorylation and suppressed EMT-associated SNAI2 expression in ESCC cells, supporting the involvement of TGF-β/SMAD/SNAI2 signaling in its tumor cell-intrinsic anti-metastatic activity. Furthermore, in a macrophage–tumor cell conditioned-medium model, PhG attenuated tumor-conditioned macrophage-associated M2-like features, reduced macrophage-derived TGF-β secretion, and diminished the paracrine pro-migratory activity of macrophage-conditioned medium toward ESCC cells.

Collectively, these findings demonstrate that PhG suppresses ESCC metastasis through coordinated regulation of tumor cell-intrinsic TGF-β/SMAD/SNAI2 signaling and macrophage-derived paracrine TGF-β signaling. These findings support the therapeutic potential of PhG in the treatment of metastatic ESCC.

Keywords: Phloroglucinol; Esophageal squamous cell carcinoma; Tumor-associated macrophages; Epithelial-mesenchymal transition; TGF-β/SMAD signaling; SNAI2 (Slug); Macrophage reprogramming; Metastasis

1.Introduction

Esophageal squamous cell carcinoma (ESCC) is one of the most aggressive malignancies, characterized by rapid progression and a high propensity for metastasis (1,2). Despite advances in multimodal therapies, the prognosis of ESCC patients remains poor, largely due to early dissemination and metastatic progression (3,4). Epithelial–mesenchymal transition (EMT) is a key biological process driving tumor invasion and metastasis, enabling epithelial cancer cells to acquire mesenchymal traits and enhanced migratory capacity (5–7). Among the signaling pathways regulating EMT, transforming growth factor-β (TGF-β) signaling plays a central role(8,9). Activation of the canonical TGF-β/SMAD2/3 pathway induces transcriptional programs that promote EMT, including the upregulation of transcription factors such as SNAI2 (Slug), which repress epithelial markers such as E-cadherin (10–12). In addition to tumor cell-intrinsic signaling, the tumor microenvironment critically contributes to EMT progression (13). Tumor-associated macrophages (TAMs), particularly those with an M2-like phenotype, are a major source of TGF-β and have been shown to promote tumor invasion and metastasis through paracrine signaling (14–16). Targeting both tumor cell-intrinsic EMT programs and microenvironment-derived signals is therefore considered a promising strategy for limiting metastatic progression (13). Phloroglucinol (PhG,1,3,5-trihydroxybenzene) is a natural polyphenolic compound widely distributed in marine algae and terrestrial plants, with established anti-inflammatory and antioxidant properties, and is clinically used as a safe antispasmodic agent (17–19). However, whether PhG can suppress ESCC progression by simultaneously targeting EMT and tumor microenvironmental signaling remains unclear.

In this study, we investigated the anti-metastatic effects of PhG in ESCC and explored the underlying mechanisms at both the tumor cell and tumor microenvironment levels. Through transcriptomic analysis and functional validation, we investigated the involvement of the TGF-β/SMAD2/3/SNAI2 signaling cascade in the anti-EMT activity of PhG. We further examined the effects of PhG on tumor-conditioned macrophage phenotype and macrophage-derived paracrine signaling using a conditioned-medium model. Molecular docking analysis was additionally performed to explore a potential interaction between PhG and TGFBR1, while changes in intracellular reactive oxygen species (ROS) were examined as a potential common pharmacological feature associated with the effects of PhG in tumor cells and macrophages. Together, these findings provide evidence that PhG suppresses ESCC metastasis through coordinated regulation of tumor cell-intrinsic TGF-β/SMAD2/3/SNAI2 signaling and macrophage-derived paracrine TGF-β signaling.

2.Materials and methods

2.1 Reagents and Antibodies

2.1.1 Chemicals and reagents

Commercial phloroglucinol (PhG) injection (Hengsheng Pharmaceutical Co., Ltd.), Cell Counting Kit-8 (Beyotime, Cat. No. C0038), Matrigel Basement Membrane Matrix (Beyotime, Cat. No. C0383), Crystal Violet Staining Solution (Beyotime, Cat. No. C0121), the lipophilic fluorescent dye DiI (Service bio, Cat. No. G1705), RNAiso Plus (Takara, Code No. 9108), PrimeScript FAST RT Reagent Kit with gDNA Eraser (Takara, Code No. RR092), TB Green® Premix Ex Taq™ II (Takara, Cat. No. RR820), RIPA Lysis Buffer System (Santa Cruz, Cat. No. sc-24948), BCA Protein Assay Kit (Beyotime, Cat. No. P0012S), One-Step PAGE Gel Fast Preparation Kit (Share Bio, Cat. No. SKV-0055), Protein Marker (Yeasen, Cat. No. 26616ES72), Super ECL Detection Reagent (Yeasen, Cat. No. 36208ES60), Phorbol 12-myristate 13-acetate (MedChemExpress, Cat. No. HY-18739). recombinant human TGF-β1 (Cisco, Cat. No. Z03411-10), TGF-β type I receptor (ALK5) specific inhibitor SB431542 (Cisco, Cat. No. 301836-41-9), TGF-β1 One-step ELISA Kit (STARTER, Cat. No. S0C3056-1×96T). Reactive oxygen species (ROS) assay kit (Adamas-life, Cat. No. C8093) were used in this study.

2.1.2 Antibodies

The primary and secondary antibodies used for Western blotting and flow cytometry analysis were as follows: E-cadherin (ELK Biotechnology, Cat. No. ES2220), Slug (ELK Biotechnology, Cat. No. ES20633), Vimentin (ELK Biotechnology, Cat. No. ES3698), N-cadherin (Bioss, Cat. No. bsm-34125M), SMAD2/3 (Cell Signaling Technology, Cat. No. 8685T), phospho-SMAD2/3 (Cell Signaling Technology, Cat. No. 8828T), β-actin (Beyotime, Cat. No. AF2811), HRP-conjugated goat anti-rabbit IgG (Beyotime, Cat. No. A0208), HRP-conjugated goat anti-mouse IgG (Beyotime, Cat. No. A0216), Fixable Viability Stain 780 (BD Biosciences, Cat. No. 565388), Zombie Aqua™ Fixable Viability Kit(Biolegend, Cat. No. 423101), APC-Cy7 anti-human CD45 (BD Biosciences, Cat. No. 561863), FITC anti-human CD11b (Absin, Cat. No. abs180027-100T), Alexa Fluor 647 anti-human CD68 (BD Biosciences, Cat. No. 562111), PE anti-human CD86 (BD Biosciences, Cat. No. 557344), and PE-Cyanine7 anti-human CD163 (Thermo Fisher Scientific, Cat. No. 25-1639-42). PE-anti-mouse F4/80(BioLegend, Cat.No.123110), PE-CF594 Rat-CD11b (BD Biosciences, Cat. No. 562287), PE-Cyanine7 Anti-MO CD206(Thermo Fisher Scientific, Cat. No. 25-2061-82),APC Anti-Mouse CD86 (proteintech, Cat. No. APC-FcA98025)

2.2 Cell lines and culture conditions

The human ESCC cell line KYSE150, murine ESCC cell line AKR, human monocytic cell line THP-1, and murine macrophage cell line RAW264.7 were obtained from the Cell Bank of the Chinese Academy of Sciences (Shanghai, China). KYSE150 and THP-1 Cells were cultured in RPMI-1640 medium，whereas AKR and RAW264.7 cells were cultured in DMEM (both from Gibco, USA). All media were supplemented with 10% fetal bovine serum (FBS; Gibco, USA), 100 U/mL penicillin, and 100 μg/mL

streptomycin. Cells were maintained at 37°C in a humidified incubator with 5% CO_2. All cell lines were routinely tested for mycoplasma contamination and confirmed to be negative.

2.3 Cell Counting Kit-8 (CCK-8) assay

The cytotoxicity of PhG and SB431542 was evaluated using a CCK-8 assay. Cells were seeded into 96-well plates at the following densities: KYSE150, 5×10^3 cells/well; AKR, 3×10^3 cells/well; THP-1, 1×10^4 cells/well; RAW264.7, 3×10^3 cells/well. After overnight incubation, cells were treated with the indicated concentrations of PhG or SB431542 for 24 or 48 h. Subsequently, the culture medium was replaced with 100 μL of fresh medium containing 10% CCK-8 reagent, and the plates were incubated at 37°C for 1–2 h in the dark. Absorbance was measured at 450 nm using a microplate reader (BioTek Instruments, Winooski, VT, USA).

2.4 Wound healing assay

Cell migration was assessed using a wound healing assay. KYSE150 and AKR cells were seeded into 6-well plates and cultured to approximately 90–95% confluence. A linear scratch was created using a sterile 200-μL pipette tip, and detached cells were removed by washing three times with PBS. Cells were subsequently cultured in medium containing 1% FBS and the indicated concentrations of PhG (0, 12.5, 25, 50, and 100 μg/mL). Images were captured at 0, 24, and 48 h using an inverted microscope (Olympus, Tokyo, Japan). Wound closure was quantified using ImageJ software (NIH, Bethesda, MD, USA), and the wound-healing rate was calculated based on the change in wound area over time.

2.5 Transwell migration and invasion assays

Transwell migration and invasion assays were performed using 24-well inserts with 8-μm pore size membranes (LabSelect, Beijing, China). For migration assays, 5×10^4 cells were suspended in 200 μL serum-free medium containing the indicated concentrations of PhG and seeded into the upper chambers. For invasion assays, 1×10^5 cells were seeded into Matrigel-coated inserts, with Matrigel diluted 1:8 in serum-free medium. The lower chambers were filled with 600 μL of complete medium containing 10% FBS as a chemoattractant. After 24 h incubation at 37°C, non-migrated or non-invaded cells on the upper surface were removed with a cotton swab. Cells on the lower surface were fixed with 4% paraformaldehyde and stained with crystal violet. Images were captured using an inverted microscope (Olympus, Tokyo, Japan), and cells were counted in five randomly selected fields per well.

2.6 RNA Extraction, Library Construction, and Sequencing

Total RNA was extracted using TRIzol® Reagent (Invitrogen, Carlsbad, CA, USA) according to the manufacturer's protocol. RNA quality was assessed using an Agilent 5300 Bioanalyzer system (Agilent Technologies, CA, USA). RNA samples meeting the required quality criteria were used for library preparation with the Illumina® Stranded

mRNA Prep, Ligation kit (Illumina, San Diego, CA, USA). Libraries were sequenced on an Illumina NovaSeq X Plus platform using paired-end 150-bp sequencing (PE150) by Shanghai Majorbio Bio-pharm Technology Co., Ltd. (Shanghai, China).

2.7 Bioinformatics Analysis

Raw paired-end sequencing reads were processed using fastp for adapter removal and quality control. Clean reads were aligned to the reference genome using HISAT2, and gene abundance was quantified using RSEM. Differential expression analysis was performed using DESeq2. Genes with a $|\log_2FC| > 1$ and FDR < 0.05 were considered differentially expressed genes (DEGs). Subsequent bioinformatics analyses were performed on the Majorbio Cloud Platform (https://cloud.majorbio.com/). To identify EMT-related targets, the DEGs were intersected with the "Hallmark Epithelial Mesenchymal Transition" gene set from the Molecular Signatures Database (MSigDB, v2025.1), and expression patterns were visualized using hierarchical clustering heatmaps. To identify the *SNAI2*-centered regulatory network, Spearman correlation coefficients (SCC) were calculated between *SNAI2* and all other DEGs. Genes satisfying the criteria of $|SCC| > 0.9$ and $|\log_2FC| > 1.5$ were identified as *SNAI2*-correlated genes. Functional annotation and transcription factor enrichment analysis of the *SNAI2*-correlated gene set were performed using the Metascape database (http://metascape.org)(20–22). This analysis included Gene Ontology (GO) enrichment, KEGG pathway analysis, and the identification of potential upstream regulators based on the TRRUST database integrated within Metascape. Terms with a P-value < 0.01, a minimum count of 3, and an enrichment factor > 1.5 were considered statistically significant. Kappa scores were used as the similarity metric when performing hierarchical clustering on the enriched terms, and sub-trees with a similarity of > 0.3 were considered as clusters.

Finally, both the SNAI2-centered co-expression network and functional enrichment results were visualized using Cytoscape software (version 3.9.0).

2.8 Quantitative real-time PCR (RT-qPCR)

Total RNA was extracted from KYSE150 cells treated with PhG (50 μg/mL) or vehicle for 24 h using RNAiso Plus (Takara, Japan). RNA concentration and purity were determined using a NanoDrop 2000 spectrophotometer (Thermo Scientific, USA). Total RNA was reverse transcribed into cDNA using the PrimeScript™ FAST RT Reagent Kit with gDNA Eraser (Takara, Japan). RT-qPCR was performed using TB Green® Premix Ex Taq™ II (Takara, Japan) on a LightCycler® 96 Real-Time PCR System (Roche, Switzerland). Relative mRNA expression levels were normalized to GAPDH. Primer sequences are listed belows.

Gene (Symbol)	Forward Primer (5′-3′)	Reverse Primer (5′-3′)

Slug (*SNAI2*)	TGTGTGGACTACCGCTGCTC	GAGGAGGTGTCAGATGGAGGAG
GAPDH (*GAPDH*)	CATGAGAAGTATGACAACAGC	AGTCCTTCCACGATACCAAAG

2.9 Western Blotting

KYSE150 and AKR cells were treated with indicated concentrations of PhG (0, 25, and 50 μg/mL) or with PhG (50 μg/mL) in combination with recombinantTGF-β(rTGF-β; 10 ng/mL) for 24 h to assess EMT-related protein expression. To evaluate TGF-β-induced SMAD2/3 phosphorylation, cells were pretreated with PhG (50 μg/mL) for 1 h and subsequently stimulated with rTGF-β (10 ng/mL) for 30 min. Total protein was extracted using RIPA lysis buffer supplemented with protease and phosphatase inhibitors. Protein concentrations were determined using a BCA assay. Equal amounts of protein were separated by 10% SDS-PAGE and transferred onto nitrocellulose membranes (Millipore, USA). Membranes were blocked with 5% non-fat milk or BSA and incubated overnight at 4°C with primary antibodies against E-cadherin (1:2000), N-cadherin (1:2000), Vimentin (1:2000), Slug (1:1000), SMAD2/3 (1:1000), p-SMAD2/3 (1:1000), and β-Actin (1:1000). After washing, membranes were incubated with corresponding HRP-conjugated secondary antibodies. Protein bands were visualized using an ECL detection system and quantified using ImageJ software. Target protein expression was normalized to β-actin, whereas phospho-SMAD2/3 was normalized to total SMAD2/3. Relative protein expression was expressed with the control group normalized to 1.

For EMT-related protein analyses, because multiple target proteins were examined, the membranes were cut into sections according to the molecular weight ranges of the target proteins before antibody incubation. Different sections from the same membrane were then incubated with the corresponding antibodies. For phosphorylation analyses, because the molecular weights of the target proteins and their loading controls were similar, the same membrane was stripped and subsequently incubated with the next antibody. As the membranes used for EMT-related protein analyses were cut before antibody incubation, uncropped images of the full-length membranes with the original membrane edges are not available. Images of the membrane sections and the corresponding independent experimental replicates are provided in the Supplementary Information.

2.10 Molecular docking

Molecular docking is a computational approach used to investigate potential receptor–ligand interactions and predict binding modes. In this study, molecular docking was performed to explore whether PhG could potentially interact with key components of the TGF-β signaling pathway. The three-dimensional structures of PhG and the

reference TGFBR1 inhibitor SB431542 were retrieved from the PubChem database (https://pubchem.ncbi.nlm.nih.gov/). The crystal structures of TGFBR1 (PDB: 1VJY), SMAD2 (PDB: 1KHX), and SMAD3 (PDB: 1MJS) were obtained from the RCSB Protein Data Bank (https://www.rcsb.org/). Prior to docking, water molecules and co-crystallized ligands were removed, and the receptor proteins were prepared by adding polar hydrogen atoms and assigning Gasteiger charges using AutoDock Tools 1.5.7. Both receptors and ligands were saved in PDBQT format.

Docking simulations were performed with the receptors treated as rigid and all rotatable bonds of the ligands allowed to rotate freely. Blind docking was first performed using grid boxes covering the protein surfaces to explore potential binding regions. Refined docking was subsequently performed within the identified binding regions and selected functional regions, including the ATP-binding region of TGFBR1 and the MH2 domains of SMAD2 and SMAD3, to further characterize the predicted binding modes. SB431542 was included as a reference TGFBR1 inhibitor for comparison with PhG. The optimal binding poses were selected based on the predicted binding energy (kcal/mol). Protein–ligand interactions were visualized and analyzed using Discovery Studio Visualizer.

2.11 Collection of conditioned media (CM) and induction of Tumor-associated macrophages (TAMs)

2.11.1 Preparation of ESCC-conditioned medium (EC-CM)

KYSE150 or AKR cells were cultured until reaching approximately 80% confluence. The cells were then washed twice with PBS and incubated in their respective media (RPMI-1640 or DMEM) supplemented with 1% FBS at 37°C for 24 h. The culture supernatants were collected and centrifuged at 500 × g for 20 min at room temperature, followed by filtration through a 0.2-μm sterile membrane to remove cellular debris. The resulting ESCC-conditioned medium (EC-CM) was aliquoted and stored at −80°C.

2.11.2 Induction of TAMs and preparation of TAM-conditioned medium

Human THP-1 monocytes were seeded into 10-cm culture dishes at a density of 6×10^5 cells/mL and treated with 50 ng/mL PMA for 24 h to induce differentiation into adherent M0 macrophages. RAW264.7 cells were used directly without PMA treatment. Following differentiation, the original medium was removed, and macrophages were incubated in polarization medium consisting of a 1:1 mixture of EC-CM and complete culture medium for 48 h to induce the TAM phenotype. To investigate the effect of PhG on macrophage polarization, M0 macrophages were co-treated with 50 μg/mL PhG during this polarization period, generating the TAM(PhG) group. After the 48-h polarization period, macrophages were thoroughly washed and cultured in fresh serum-free medium for an additional 24 h to collect the secreted factors. The supernatants were collected, centrifuged at 500 × g for 20 min at room temperature, and filtered through a 0.2-μm membrane. The resulting M0-CM, TAM-CM, and TAM(PhG)-CM were

aliquoted and stored at −80°C until further use. A schematic overview of this workflow is shown in Fig. 5A.

2.12 Flow cytometry

THP-1-derived macrophages were stained with Zombie Aqua™ Fixable Viability Dye to exclude dead cells. Following Fc receptor blocking, cells were surface stained with anti-CD11b and anti-CD68 antibodies, fixed, permeabilized, and subsequently stained intracellularly with anti-CD86 and anti-CD163 antibodies. RAW264.7 macrophages were stained with Fixable Viability Stain 780, followed by surface staining with anti-CD11b and anti-F4/80 antibodies and intracellular staining with anti-CD86 and anti-CD206 antibodies. Data were acquired on a NovoCyte flow cytometer (Agilent Technologies, USA) and analyzed using NovoExpress software (version 1.5).

2.13 Enzyme-Linked Immunosorbent Assay (ELISA)

Secreted TGF-β levels in macrophage-derived CM, including M0-CM, TAM-CM, and TAM(PhG)-CM, were quantified using TGF-β1 One-step ELISA Kit. Absorbance was measured at 450 nm, and cytokine concentrations were calculated based on the standard curve.

2.14 Intracellular ROS measurement

Intracellular ROS levels were determined using a Reactive oxygen species assay kit. Following the indicated treatments, KYSE150 cells, AKR cells, THP-1-derived macrophages, and RAW264.7 macrophages were incubated with 10 μM DCFH-DA for 20 min at 37 °C in the dark according to the manufacturer's instructions. Cells were subsequently washed to remove excess probe, and intracellular fluorescence was analyzed using a NovoCyte flow cytometer (Agilent Technologies, USA). ROS levels were quantified based on the mean fluorescence intensity (MFI) using NovoExpress software (version 1.5).

2.15 Animals

2.15.1 Zebrafish xenograft model

Wild-type AB strain zebrafish were obtained from the Zebrafish Platform of the School of Basic Medical Sciences, Southwest Medical University, China, and maintained in a recirculating aquaculture system at 28.0 ± 0.5°C under a standard 14-h light/10-h dark photoperiod. Embryos were obtained by natural mating and maintained in standard E3 medium at 28.5°C. Healthy larvae at 48 hours post-fertilization (hpf) were selected for subsequent experiments. Larvae were anesthetized with 0.016% tricaine methanesulfonate (MS-222) when required and euthanized at the end of the experiments by an overdose of tricaine. All zebrafish procedures were performed in accordance with institutional animal care guidelines and relevant national regulations(23).

Experiments were terminated prior to the onset of independent feeding and before 120 hpf, consistent with current ethical recommendations for zebrafish research(24).

Healthy larvae were first used to evaluate the developmental toxicity of PhG by assessing survival, gross morphology, body length, heart rate, and touch-evoked escape response. A separate cohort of larvae was subsequently used to establish the zebrafish xenograft model. KYSE150 cells were labeled with the lipophilic fluorescent dye DiI and microinjected into the perivitelline space of dechorionated embryos at 48 hpf (approximately 200–400 cells per larva). Larvae with successful engraftment were randomly assigned to treatment groups (n = 15 per group) and incubated in E3 medium containing PhG (0, 25, or 50 μg/mL) for 48 h. Tumor dissemination was monitored at 72 and 96 hpf using a fluorescence stereomicroscope (Olympus MVX10, Japan).

2.15.2 Mouse Footpad tumor model

Female C57BL/6 mice (6 weeks old) were obtained from the Animal Experimental Center of Southwest Medical University, China, and maintained under specific pathogen-free (SPF) conditions with free access to food and water. AKR cells (1×10^6 cells in 25 μL PBS) were inoculated into the right hind footpad of each mouse **u**nder mild anesthesia induced by 2% isoflurane. When tumors were 2 ~ 3 mm in diameter, the mice were randomly divided into three groups (n = 5 per group): a vehicle control group and two PhG treatment groups (10 mg/kg and 25 mg/kg). PhG or vehicle was administered via intraperitoneal injection every other day for 14 days. To comply with animal welfare guidelines, tumor-bearing animals were euthanized before the footpad thickness reached the ethical limit of 5 ~ 6 mm. Euthanasia was performed by cervical dislocation following anesthesia with 4% isoflurane to ensure the animals were completely unconscious and insentient. Primary tumor tissues from the footpads and ipsilateral popliteal and inguinal lymph nodes were collected. H&E staining was performed to identify and confirm metastatic lesions in the lymph nodes.

2.16 Statistical analysis

Data are presented as the mean ± standard deviation (SD). Statistical analyses were performed using GraphPad Prism software (version 10.0; GraphPad Software, San Diego, CA, USA). Comparisons between two groups were performed using an unpaired two-tailed Student's *t*-test, whereas comparisons among multiple groups were analyzed by one-way analysis of variance (ANOVA) followed by Tukey's multiple comparisons test. Differences were considered statistically significant at $P < 0.05$.

3.Results

3.1 Phloroglucinol (PhG) inhibits the migration and invasion of ESCC cells at non-cytotoxic concentrations

First, the effects of PhG on the viability of human ESCC KYSE150 cells and murine esophageal cancer AKR cells were evaluated using the CCK-8 assay. The results showed that treatment with PhG at concentrations up to 100 μg/mL for 24 h and 48 h did not significantly reduce cell viability in either cell line (**Fig. 1B, C**). No IC_{50} was reached within the tested concentration range. in both cell lines, indicating a broad non-

cytotoxic concentration range. Based on these results, concentrations within the 0–100 μg/mL range were used for subsequent functional assays, with specific concentrations selected according to the experimental design.

Subsequently, given the aggressive nature of ESCC(25), we performed wound-healing assays to specifically evaluate the impact of PhG on the motility of both KYSE150 and AKR cells. The results revealed that PhG significantly inhibited migration of both KYSE150 and AKR cells in a dose-dependent manner. Treatment with 50 μg/mL PhG significantly delayed wound closure at 24 h ($P < 0.05$), and no further significant inhibition was observed at 100 μg/mL (**Fig. 1D-G**). To corroborate these observations, we performed Transwell assays. Consistent with the wound-healing results, Transwell assays demonstrated that PhG markedly reduced the number of migrating cells. Similarly, in Matrigel-coated Transwell assays, PhG significantly impaired the invasive capacity of both KYSE150 and AKR cells (Fi**g. 1H, I**).

Collectively, these findings demonstrate that PhG suppresses the migratory and invasive capacities of ESCC cells in vitro at concentrations that do not cause overt loss of cell viability.

3.2 PhG Inhibits Metastasis of ESCC Cells *in vivo*

To further validate the anti-metastatic effect of PhG *in vivo*, we employed both a zebrafish xenograft model and a mouse footpad tumor model.

In the zebrafish model, we first evaluated the *in vivo* biosafety of PhG. Zebrafish larvae at 48 hpf were exposed to PhG at concentrations of 0, 25, and 50 μg/mL for 48 h. Morphological examination revealed that PhG treatment induced no overt developmental abnormalities, including pericardial edema or spinal curvature, with larvae exhibiting normal developmental features comparable to the control (**Fig. 2A**). Consistently, body length measurements showed no significant developmental delay (**Fig. 2B**). Survival rates exceeded 95% across all groups, indicating no evident treatment-related lethality. (**Fig. 2C**). In addition, PhG treatment did not significantly affect cardiac function (heart rate, **Fig. 2D**) or neuromuscular activity (touch-evoked escape behavior, **Fig. 2E**). These findings indicate that PhG exhibits a favorable *in vivo* safety profile at the tested concentrations.

We next assessed the effect of PhG on tumor metastasis *in vivo*. DiI-labeled KYSE150 cells were microinjected into the perivitelline space of zebrafish larvae at 48 hpf, followed by PhG treatment. Tumor cell dissemination was monitored by fluorescence imaging at 48, 72, and 96 hpf. In the control group, progressive metastatic spread was observed, with tumor cells migrating from the injection site toward the distal tail region as early as 72 hpf **(Fig. 2F)**. In contrast, PhG treatment significantly and dose-dependently reduced metastatic dissemination at both the 72 hpf and 96 hpf **(Fig. 2G)**.

To further evaluate the effect of PhG on metastatic dissemination in a mammalian model, we established a footpad tumor model using the murine esophageal carcinoma

cell line AKR. Evaluation of the number of metastases in the ipsilateral popliteal and inguinal lymph nodes revealed that, compared with the vehicle control group, PhG treatment significantly suppressed tumor metastasis to these regional lymph nodes (**Fig. 2H and I**). To further validate the macroscopic findings from a pathological perspective, lymph nodes were examined by H&E staining. At low magnification (4×), the overall architecture of the lymph nodes remained identifiable. At higher magnification (20×), tumor cells were clearly observed breaching the lymph node capsule and infiltrating the subcapsular sinus, with a more extensive distribution of tumor cells in the control group than in PhG-treated mice (**Fig. 2J**). These histological findings confirmed that the macroscopically enlarged lymph nodes represented metastatic tumor lesions rather than simple reactive lymph node enlargement.

Collectively, these results demonstrate that PhG effectively suppresses the *in vivo* metastasis of ESCC, which is consistent with our *in vitro* findings.

3.3 Transcriptome profiling identifies SNAI2 and implicates TGF-β signaling in PhG-mediated EMT regulation

To explore the molecular mechanisms underlying the anti-migratory activity of PhG, we performed RNA-seq analysis on KYSE150 cells treated with 50 μg/mL PhG for 24 h, a condition selected based on the preliminary functional assays. Using thresholds of $|\log2FC| > 1$ and FDR < 0.05, we identified 3,474 differentially expressed genes (DEGs), including 1,745 downregulated and 1,729 upregulated genes (**Fig. 3A**). Given the pronounced inhibitory effect of PhG on cell migration, we next focused on EMT-related genes. Intersection with the Hallmark EMT gene set (MSigDB) identified 26 EMT-associated DEGs responsive to PhG treatment (**Fig. 3B**). Among these, SNAI2, a key transcriptional regulator of EMT, was markedly downregulated, as shown by hierarchical clustering (**Fig. 3C**). This finding was further validated by RT-qPCR, confirming a significant reduction in SNAI2 mRNA levels following PhG treatment (**Fig. 3D**). To further investigate the regulatory context of SNAI2, we analyzed genes co-expressed with SNAI2 within the DEGs. Using stringent criteria ($|R| > 0.9$ and $|\log2FC| > 1.5$), 121 genes were identified as strongly correlated with SNAI2 (**Fig. 3E**). Functional enrichment analysis revealed that these genes were predominantly associated with biological processes related to cell adhesion, cell migration, and EMT. Notably, pathway enrichment analysis also identified significant enrichment of the TGF-β signaling pathway within this gene set, suggesting a potential connection between SNAI2-associated transcriptional changes and TGF-β signaling (**Fig. 3G**). In addition, transcriptional regulatory analysis suggested enrichment of MYC-associated targets within this gene set (**Fig. 3F**), further supporting a potential link between SNAI2-associated transcriptional programs and TGF-β signaling.

Collectively, these transcriptomic analyses identified SNAI2 as a prominent PhG-responsive EMT-associated gene and implicated TGF-β signaling as a potential pathway associated with its regulation.

3.4 Phloroglucinol attenuates TGF-β-induced EMT in ESCC cells through modulation of the SMAD2/3/SNAI2 signaling cascade

Prompted by the bioinformatics findings, we next investigated whether PhG functionally modulates the EMT program in ESCC by evaluating EMT markers(E-cadherin, N-cadherin, Vimentin) (26,27). Western blot analysis demonstrated that PhG treatment for 24 h increased the expression of the epithelial marker E-cadherin, while decreasing the mesenchymal markers N-cadherin, Vimentin, and the transcription factor Slug in KYSE150 cells in a dose-dependent manner (**Fig. 4A-E)**, indicating suppression of EMT.

Given that TGF-β is a canonical inducer of EMT (8,9) and a key signaling node identified in our RNA-seq data, we next evaluated whether PhG could antagonize exogenous TGF-β-driven EMT responses. Cells were treated with TGF-β in the presence or absence of PhG for 24 h. As expected, treatment with exogenous TGF-β promoted EMT, as evidenced by decreased E-cadherin and increased N-cadherin, Vimentin, and Slug expression, accompanied by enhanced cell migration. Notably, co-treatment with PhG markedly attenuated TGF-β-induced EMT changes, partially restoring epithelial marker expression while suppressing mesenchymal markers and cell migration (**Fig.4F-J, T, U**).

We next examined whether the inhibitory effect of PhG on TGF-β-induced EMT was associated with modulation of canonical SMAD signaling. KYSE150 Cells were pretreated with PhG for 1 h and subsequently stimulation with rTGF-β (10 ng/mL) for 30 min, a time point reported to robustly detect TGF-β-induced SMAD2/3 phosphorylation (28–30). rTGF-β stimulation markedly increased SMAD2/3 phosphorylation, whereas PhG pretreatment attenuated this response. In contrast, the total SMAD2/3 protein levels remained largely unchanged across different treatment conditions, indicating that PhG attenuates TGF-β-induced SMAD2/3 phosphorylation without substantially altering total SMAD2/3 protein levels. (**Fig. 4F, K, L**). Similar effects were observed in the murine esophageal cancer cell line AKR (**Fig. 4M-S, V, W**).

Collectively, these findings demonstrate that PhG attenuates TGF-β-induced EMT and associated cell migration, accompanied by suppression of SMAD2/3 phosphorylation and reduced Slug expression. Together with the transcriptomic findings, these results support the involvement of the TGF-β/SMAD2/3/SNAI2 signaling cascade in the anti-migratory effects of PhG in ESCC cells.

3.5 Molecular docking suggests a potential interaction between PhG and TGFBR1

Given that PhG markedly attenuated TGF-β-induced SMAD2/3 phosphorylation and EMT in ESCC cells, we further investigated whether PhG could potentially interact with key components of the TGF-β/SMAD signaling pathway. TGFBR1 was selected as the primary receptor target because, following activation of the TGF-β receptor complex, it mediates the phosphorylation of receptor-regulated SMAD2/3, whereas TGFBR2 primarily functions to activate TGFBR1(31). Molecular docking analyses were therefore performed to evaluate the potential interactions of PhG with TGFBR1, SMAD2, and SMAD3.

As a reference compound, the known TGFBR1 inhibitor SB431542 was first docked against TGFBR1 under the same computational framework. SB431542 exhibited a favorable predicted binding energy of −10.97 kcal/mol, with predicted interactions involving Lys232, Asp351, Val219, Leu340, and Ala230, primarily through π-sigma and π-alkyl interactions **(Fig. 5A; Table 1).** The predicted interaction of SB431542 with the TGFBR1 kinase domain was consistent with its established pharmacological activity as a TGFBR1 inhibitor, providing a structural reference for comparison with the predicted binding mode of PhG. Using the same docking protocol, PhG showed a predicted binding energy of −6.093 kcal/mol with TGFBR1, representing the most favorable predicted docking score among the tested PhG–protein models. PhG was predicted to interact with Tyr378, Arg332, Ala399, and Ala403, with additional contacts involving Asp400, Leu334, Asp333, Thr375, Met379, Gly374, Ala380, and Val383. These interactions mainly involved amide–π stacking, π-alkyl, and van der Waals interactions **(Fig. 5B; Table 1).** Notably, the predicted binding region of PhG was spatially distinct from that occupied by SB431542 **(Fig. 5A, B)**, suggesting that PhG may interact with TGFBR1 through a binding mode distinct from that of the reference inhibitor.

We further examined the potential interactions of PhG with the downstream signaling proteins SMAD2 and SMAD3. PhG exhibited predicted binding energies of −4.964 and −4.225 kcal/mol with SMAD2 and SMAD3, respectively. The predicted interactions involved multiple residues within the respective proteins and included π–π, π-alkyl, π-cation, and van der Waals interactions **(Fig. 5C, D; Table 1)**. Compared with TGFBR1, both SMAD2 and SMAD3 showed less favorable predicted docking scores under the same computational framework. These findings suggested that, among the tested TGF-β/SMAD signaling components, TGFBR1 represented a potentially more favorable interaction site for PhG and therefore provided a rationale for further considering TGFBR1 as a potential upstream site of action.

Collectively, these molecular docking results indicate that TGFBR1 is the most likely direct target of PhG among the tested components of the TGF-β/SMAD signaling pathway. Together with the experimental evidence that PhG inhibits TGF-β-induced SMAD2/3 phosphorylation and EMT, these findings suggest that a potential interaction

between PhG and TGFBR1 may help explain the inhibitory effects of PhG on TGF-β/SMAD signaling in ESCC cells.

3.6 Phloroglucinol attenuates macrophage-mediated ESCC cell migration by reducing TAM-derived TGF-β secretion

Having established that PhG attenuates TGF-β/SMAD signaling in ESCC cells, we next investigated whether PhG could also modulate tumor-conditioned macrophage function and thereby affect macrophage–tumor cell crosstalk. Because TAMs are an important source of TGF-β within the tumor microenvironment and can promote tumor cell motility through paracrine signaling (32–34), we established a conditioned medium (CM)-based model to examine the effects of PhG on macrophage phenotype and macrophage-mediated tumor cell migration.

A schematic overview of the generation of macrophage-derived CM under the indicated treatment conditions is shown in **Fig. 6A**. To exclude potential cytotoxic effects of PhG on macrophages, cell viability was first assessed by CCK-8 assay. Treatment with PhG at concentrations up to 100 μg/mL for 48 h did not significantly affect the viability of either THP-1-derived macrophages or RAW264.7 cells (**Fig. 6B, C**).

We next examined whether PhG modulated the phenotype of macrophages exposed to ESCC-conditioned medium. THP-1-derived macrophages stimulated with ESCC-conditioned medium developed an elongated, spindle-shaped morphology characteristic of tumor-conditioned macrophages, whereas the addition of PhG resulted in a more rounded cellular morphology (**Fig. 6D**). Flow cytometric analysis further demonstrated that ESCC-conditioned medium significantly increased both the proportion and median fluorescence intensity (MFI) of CD163-positive macrophages. Co-treatment with PhG reduced the CD163-positive population and its MFI, accompanied by an increase in CD86 expression (**Fig. 6E**). These findings indicate that PhG attenuates the M2-associated phenotypic features induced by tumor-conditioned stimulation while promoting a relative shift toward a CD86-expressing phenotype.

A similar phenotypic trend was observed in RAW264.7 macrophages exposed to ESCC-conditioned medium (**Fig. 6F, G**). However, changes in the MFI of CD86 and CD206 did not reach statistical significance, indicating that the effects of PhG on macrophage phenotype were less pronounced in RAW264.7 cells than in THP-1-derived macrophages.

We next examined whether PhG-induced phenotypic changes were accompanied by alterations in TGF-β secretion. ELISA analysis showed that TGF-β levels were markedly increased in conditioned medium collected from tumor-conditioned macrophages compared with M0 macrophage-derived CM. Notably, treatment of macrophages with PhG substantially reduced TGF-β levels in the resulting conditioned medium, approaching those detected in the M0 control (**Fig. 6H**). These findings

suggest that PhG suppresses the enhanced TGF-β secretory activity induced by tumor-conditioned stimulation.

Changes in TGF-β levels within the tumor microenvironment can affect the migratory capacity of cancer cells. To verify this hypothesis, cancer cells were co-cultured with CM derived from macrophages under different conditions, and their migratory capacity was evaluated using a wound-healing assay. After 24 h of culture, TAM-CM significantly promoted cancer cell migration, whereas TAM-CM derived from PhG-treated macrophages substantially attenuated this pro-migratory effect, resulting in a wound closure rate comparable to that of the control group (Fig. 6J). Considering that TAM-CM contains multiple components, including TGF-β (35,36), we further investigated whether the anti-migratory effect produced by PhG treatment of TAMs was associated with inhibition of the TGF-β signaling pathway. To this end, the TGF-β type I receptor (ALK5) inhibitor SB431542 was used as a positive control for validation. First, the potential effect of SB431542 on cell viability was excluded by a CCK-8 assay. SB431542, at concentrations of up to 20 μM for 24 h, did not cause apparent cytotoxicity in ESCC cells (**Fig. 6I**). We then performed a wound-healing assay. SB431542 (2.5 μM) effectively attenuated the pro-migratory effect induced by TAM-CM, producing a migration phenotype similar to that of the PhG-treated TAM-CM group (**Fig. 6J, K**). further supporting that PhG attenuates the pro-migratory activity of TAMs by suppressing TAM-derived TGF-β signaling. Similar results were obtained in mouse-derived macrophage and ESCC cell models, further confirming the robustness of these findings (**Fig. 6L-O**).

Collectively, these results indicate that PhG modulates the phenotypic characteristics of TAMs under tumor-conditioned stimulation and reduces their TGF-β secretion, thereby attenuating the paracrine pro-migratory effect of TAM-derived CM on ESCC cells.

3.7 Phloroglucinol attenuates intracellular ROS accumulation in ESCC cells and macrophages.

Given that oxidative stress has been implicated in both EMT activation in tumor cells and macrophage functional polarization (37,38), we next examined whether the pharmacological effects of PhG were associated with alterations in intracellular ROS levels. Flow cytometric analysis showed that exogenous TGF-β markedly increased intracellular ROS levels in both KYSE150 and AKR cells, whereas PhG treatment significantly attenuated ROS accumulation under both basal and TGF-β-stimulated conditions (**Fig. 7A-D**). Similarly, conditioned medium derived from ESCC cells induced ROS accumulation in THP-1-derived macrophages and RAW264.7 cells, while PhG markedly reduced intracellular ROS levels in both macrophage models (**Fig. 7E-H**). Collectively, these findings demonstrate that PhG attenuates intracellular ROS accumulation in both ESCC cells and macrophages, suggesting that suggesting that

suppression of intracellular oxidative stress may represent a common pharmacological feature associated with its effects on both tumor cells and the tumor microenvironment.

4.Discussion

Esophageal squamous cell carcinoma (ESCC) remains one of the lethal malignancies worldwide, largely owing to its aggressive progression and high metastatic potential(2). Metastatic dissemination is driven by coordinated interactions between tumor cell-intrinsic signaling programs and the tumor microenvironment, with EMT representing an important component of this process(10,39–41). Whether PhG can exert anti-metastatic activity through effects on both compartments in ESCC remains unclear. In the present study, we demonstrate that PhG suppresses ESCC metastasis through coordinated inhibition of tumor cell-intrinsic TGF-β/SMAD/SNAI2 signaling and macrophage-derived paracrine TGF-β signaling.

The present study identifies the canonical TGF-β/SMAD2/3/SNAI2 signaling cascade as a key mechanism contributing to the tumor cell-intrinsic anti-metastatic effects of PhG in ESCC. As an important EMT transcription factor, SNAI2 integrates extracellular signaling to promote epithelial plasticity and metastatic dissemination (42). Transcriptomic profiling revealed that SNAI2 was prominently downregulated following PhG treatment, while enrichment analyses of SNAI2-associated genes linked this transcriptional program to cell adhesion, migration, EMT, and TGF-β signaling. These findings suggest that SNAI2 may represent an important downstream effector through which altered TGF-β signaling influences the EMT phenotype. The role of canonical TGF-β/SMAD signaling in EMT and metastatic progression is well established, and numerous natural compounds suppress metastasis through inhibition of this pathway(43–45). This mechanistic hypothesis was further supported by functional experiments demonstrating that PhG selectively attenuated TGF-β-induced SMAD2/3 phosphorylation without affecting total SMAD2/3 protein levels, indicating that PhG primarily interferes with ligand-dependent activation of the canonical TGF-β pathway. Together, these findings establish the TGF-β/SMAD2/3/SNAI2 axis as the principal mechanism underlying the anti-EMT activity of PhG in ESCC. However, previous studies in breast cancer suggested that PhG inhibits SNAI2 predominantly through the PI3K/AKT and RAS/RAF/ERK pathways (46,47). This mechanistic divergence suggests that the anti-EMT activity of PhG is likely tumor-context dependent and may be context dependent and influenced by the dominant signaling networks in different tumor types.

TGFBR1 is a key upstream component of the canonical TGF-β signaling pathway and mediates SMAD2/3 phosphorylation following receptor activation(31), making it a biologically plausible potential site of action that may contribute to the modulation of ligand-induced TGF-β signaling by PhG observed in our ESCC models. Molecular docking analysis predicted a potential interaction between PhG and TGFBR1, with a

predicted binding region distinct from that of SB431542, suggesting that PhG may affect TGFBR1 through a binding mode different from that of conventional TGFBR1 inhibitors. However, molecular docking provides only a computational hypothesis of ligand–protein interactions rather than direct evidence of target engagement. Therefore, the potential interaction between PhG and TGFBR1 requires further experimental validation.

Beyond its direct effects on tumor cells, PhG also remodels the tumor microenvironment through modulation of TAMs. TAMs are widely recognized as key regulators of tumor progression through the secretion of multiple cytokines(42–44), including TGF-β, whereas functional reprogramming of TAMs has emerged as an effective strategy for suppressing tumor progression (51–53). Our study found that PhG attenuated M2-like macrophage-associated features in macrophages exposed to tumor-conditioned medium, as reflected by reduced CD163/CD206 expression and increased CD86 expression, accompanied by a marked reduction in TGF-β secretion. By mimicking the tumor microenvironment through co-culture of cancer cells with CM derived from macrophages under different conditions, we observed that TAM-derived CM promoted cancer cell migration, whereas CM derived from PhG-treated macrophages substantially attenuated this pro-migratory effect. Furthermore, pharmacological inhibition of TGF-β signaling with SB431542 produced a migration phenotype similar to that induced by CM from PhG-treated macrophages, supporting the notion that the anti-migratory activity of CM derived from PhG-treated macrophages is closely associated with inhibition of TGF-β signaling. These findings are consistent with previous studies showing that modulation of macrophage function by natural compounds can reduce TGF-β secretion and subsequently attenuate the pro-migratory and EMT-promoting effects of macrophage-derived CM. For example, astragaloside IV has been reported to inhibit M2-like macrophage polarization and reduce TGF-β levels, while CM derived from treated macrophages suppressed cervical cancer cell migration and EMT, accompanied by attenuation of TGF-β/SMAD2/3 signaling(54). In addition, another study of a natural product showed that modulation of TAM-associated microenvironmental signaling, and secretory activity could reduce malignant tumor cell behavior(55), further supporting the feasibility of targeting macrophage–tumor cell paracrine communication to restrain tumor progression. Taken together, these findings suggest that, within the tumor microenvironment, PhG may exert its anti-migratory effects by suppressing TAM-mediated paracrine TGF-β signaling, thereby reducing the pro-migratory activity of TAMs toward ESCC cells.

The coordinated inhibitory effects of PhG on both tumor cells and TAMs prompted us to consider whether these apparently distinct biological activities might be linked by a common upstream mechanism. Excessive intracellular ROS accumulation not only facilitates TGF-β-dependent EMT signaling in tumor cells(56,57) but also promotes immunosuppressive macrophage polarization within the tumor microenvironment(58,59). Moreover, alleviation of oxidative stress within the tumor microenvironment has been shown to mitigate immunosuppression and enhance the

efficacy of cancer immunotherapy (60,61). Consistent with this concept, numerous naturally derived compounds suppress EMT activation, attenuate the immunosuppressive functions of macrophages, and ultimately inhibit tumor progression and metastasis through reduction of oxidative stress(62–66). Given the well-established antioxidant properties of PhG, attenuation of intracellular ROS accumulation may represent a shared pharmacological feature associated with its effects on both tumor cells and the tumor microenvironment. As expected, PhG markedly reduced intracellular ROS accumulation in both ESCC cells and TAMs. Notably, PhG also attenuated the increase in intracellular ROS accumulation induced by exogenous TGF-β, suggesting a potential link between its redox-regulatory activity and modulation of TGF-β-responsive signaling. Although the present study did not directly establish a causal relationship between ROS attenuation and inhibition of TGF-β signaling or macrophage functional modulation, these findings indicate that attenuation of intracellular ROS is a shared pharmacological feature of PhG in both tumor cells and macrophages. Whether this redox-modulatory effect contributes causally to the regulation of TGF-β signaling or macrophage function remains to be determined.

Nevertheless, several limitations should be acknowledged. Although our findings suggest that attenuation of oxidative stress may represent a shared pharmacological feature and potential mechanistic component linking the dual effects of PhG, this hypothesis was not directly validated by causal mechanistic intervention. In addition, although molecular docking suggested a potential interaction between PhG and TGFBR1, direct target engagement and the functional relevance of this predicted interaction remain to be experimentally established. Moreover, the conditioned-medium model primarily recapitulates soluble paracrine communication and cannot fully reproduce the cellular and molecular complexity of the tumor microenvironment. Future studies should clarify the causal role of ROS, experimentally validate TGFBR1 as a potential molecular target, and confirm the identified mechanisms in vivo, while further assessing the translational potential of PhG for metastatic ESCC.

5. Conclusion

In conclusion, the present study demonstrates that PhG exerts dual anti-metastatic effects in ESCC through coordinated regulation of tumor cell-intrinsic signaling and the tumor microenvironment. Mechanistically, PhG suppresses EMT through inhibition of the TGF-β/SMAD2/3/SNAI2 signaling axis and modulates tumor-associated macrophage function, accompanied by reduced macrophage-derived paracrine TGF-β secretion. These findings support the therapeutic potential of PhG for the treatment of metastatic ESCC. (Graphical abstract)

Author Contributions Statement

C.W. and S.N. conceived and designed the study. **C.W.** performed the experiments, analyzed the data, and drafted the manuscript**. S.N. and C.W.** revised the manuscript**. T.X., X.S., and Y.L.** contributed to data collection and analysis. **Y.Y. and W.X.** provided software and resources. **L.L. and Q.L.** contributed to software development and investigation. **Q.Y. and W.M.** supervised the study, **Q.Y., S.N. and W.M.** secured funding. All authors reviewed and approved the final manuscript.

Funding

This work was supported by Sichuan Science and Technology Program (2025ZNSFSC0659), Pengzhou People's Hospital – Southwest Medical University Science and Technology Strategic Cooperation Project (2025PZXNYD18), Luzhou Science and Technology Program (2024SYF128); Science and Technology Development Fund, Macau SAR (0075/2024/RIB2 and 0003/2025/NRP)

Ethics declaration

All methods were carried out in accordance with relevant guidelines and regulations.

Animal subject

This study was conducted in accordance with the ARRIVE (Animal Research: Reporting of In Vivo Experiments) guidelines. This study was approved by the Southwest Medical University Laboratory Animal Ethics Committee. (Approval No. 20230630-003).

Declaration of competing interest

The authors confirm that there are no known financial or personal conflicts of interest that could have influenced the work reported in this paper.

Declaration of generative AI

During the preparation of this work, the authors used ChatGPT (OpenAI) solely for language editing and English language polishing. The scientific content, study design, experimental procedures, data collection and analysis, interpretation of the results, and conclusions were developed and performed by the authors. The authors reviewed and edited the AI-assisted output as necessary and take full responsibility for the content of the published article.

Data availability

RNA-Seq data were deposited into the Gene Expression Omnibus database under accession number GSE350765 and are available at the following URL: https://www.ncbi.nlm.nih.gov/geo/query/acc.cgi?acc=GSE350765. Reviewer token: ohkpyuectvedryl

Abbreviations

The following abbreviations are used in this manuscript:

PhG	Phloroglucinol
ESCC	Esophageal squamous cell carcinoma

TAMs	Tumor-associated macrophages
TGF-β	Transforming growth factor-beta
EMT	Epithelial–mesenchymal transition
CCK-8	Cell Counting Kit-8
CM	conditioned media
ROS	reactive oxygen species

References

1. Zhao YX, Zhao HP, Zhao MY, Yu Y, Qi X, Wang JH, et al. Latest insights into the global epidemiological features, screening, early diagnosis and prognosis prediction of esophageal squamous cell carcinoma. World J Gastroenterol. 2024 May 28;30(20):2638–56. doi:10.3748/wjg.v30.i20.2638

2. Bray F, Laversanne M, Sung H, Ferlay J, Siegel RL, Soerjomataram I, et al. Global cancer statistics 2022: GLOBOCAN estimates of incidence and mortality worldwide for 36 cancers in 185 countries. CA Cancer J Clin. 2024 May;74(3):229–63. doi:10.3322/caac.21834

3. Shi Y, Ge X, Ju M, Zhang Y, Di X, Liang L. Circulating Tumor Cells in Esophageal Squamous Cell Carcinoma – Mini Review. Cancer Manag Res. 2021 Nov;Volume 13:8355–65. doi:10.2147/CMAR.S337489

4. Kok VC, Lee CK, Wang MC, Lu YT. Alterations in HMGB1, ROS1, FGFR1, FGFR2, IL6, and TLR4 are associated with worse survival in patients with esophageal squamous cell carcinoma. Współczesna Onkol. 2025;29(1):99–106. doi:10.5114/wo.2025.149138

5. Dong A, Blanpain C. Identification, functional insights and therapeutic targeting of EMT tumour states. Nat Rev Cancer. 2026 Jan;26(1):8–26. doi:10.1038/s41568-025-00873-0

6. Yeung KT, Yang J. Epithelial–mesenchymal transition in tumor metastasis. Mol Oncol. 2017 Jan;11(1):28–39. doi:10.1002/1878-0261.12017

7. Mittal V. Epithelial Mesenchymal Transition in Tumor Metastasis. Annu Rev Pathol Mech Dis. 2018 Jan 24;13(1):395–412. doi:10.1146/annurev-pathol-020117-043854

8. Hao Y, Baker D, Ten Dijke P. TGF-β-Mediated Epithelial-Mesenchymal Transition and Cancer Metastasis. Int J Mol Sci. 2019 Jun 5;20(11):2767. doi:10.3390/ijms20112767

9. Lee JH, Massagué J. TGF-β in developmental and fibrogenic EMTs. Semin Cancer Biol. 2022 Nov;86:136–45. doi:10.1016/j.semcancer.2022.09.004

10. Ghantous Y, Mozalbat S, Nashef A, Abdol-Elraziq M, Sudri S, Araidy S, et al. EMT Dynamics in Lymph Node Metastasis of Oral Squamous Cell Carcinoma. Cancers. 2024 Mar 18;16(6):1185. doi:10.3390/cancers16061185

11. Liu J, Wang Y, Tang C, Zhang L, Xiong S, Wang J, et al. TGF-β in tumor development and progression: mechanisms and therapeutics. Mol Biomed. 2026 Jan 30;7(1):9. doi:10.1186/s43556-026-00403-w

12. Guo H, Hu Z, Yang X, Yuan Z, Wang M, Chen C, et al. Smad4 regulates TGF-β1-mediated hedgehog activation to promote epithelial-to-mesenchymal transition in pancreatic cancer cells by suppressing Gli1 activity. Comput Struct Biotechnol J. 2024 Dec;23:1189–200. doi:10.1016/j.csbj.2024.03.010

13. Glaviano A, Lau HSH, Carter LM, Lee EHC, Lam HY, Okina E, et al. Harnessing the tumor microenvironment: targeted cancer therapies through modulation of epithelial-mesenchymal transition. J Hematol OncolJ Hematol Oncol. 2025 Jan 13;18(1):6. doi:10.1186/s13045-024-01634-6

14. Zhang Q, Sioud M. Tumor-associated macrophage subsets: shaping polarization and targeting. Int J Mol Sci. 2023 Apr 19;24(8):7493. doi:10.3390/ijms24087493

15. Yang K, Xie Y, Xue L, Li F, Luo C, Liang W, et al. M2 tumor-associated macrophage mediates the maintenance of stemness to promote cisplatin resistance by secreting TGF-β1 in esophageal squamous cell carcinoma. J Transl Med. 2023 Jan 14;21(1):26. doi:10.1186/s12967-022-03863-0

16. Gratchev A. TGF-β signalling in tumour associated macrophages. Immunobiology. 2017 Jan 1;INNATE IMMUNITY & CANCER222(1):75–81. doi:10.1016/j.imbio.2015.11.016

17. Balhara P, Sharma S, Vasudeva N. Unraveling the chemistry, pharmacological activities, and medicinal utilization of phloroglucinol: A comprehensive review. Pharmacol Res - Nat Prod. 2025 Dec 1;9:100421. doi:10.1016/j.prenap.2025.100421

18. Corvino A, Magli E, Minale M, Autelitano A, Valente V, Pierantoni GM. Phloroglucinol-derived medications are effective in reducing pain and spasms of urinary and biliary tracts: results of phase 3 multicentre, open-label, randomized, comparative studies of clinical effectiveness and safety. Adv Ther. 2023 Feb;40(2):619–40. doi:10.1007/s12325-022-02347-3

19. Keramaris KE, Konstantopoulos K, Margaritis LH, Velentzas AD, Papassideri IS, Stravopodis DJ. Exploitation of drosophila choriogenesis process as a model cellular system for assessment of compound toxicity: the phloroglucinol paradigm. Sci Rep. 2020 Jan 14;10(1):242–54. doi:10.1038/s41598-019-57113-3

20. Zhou Y, Zhou B, Pache L, Chang M, Khodabakhshi AH, Tanaseichuk O, et al. Metascape provides a biologist-oriented resource for the analysis of systems-level datasets. Nat Commun. 2019 Apr 3;10(1):1523. doi:10.1038/s41467-019-09234-6 PubMed PMID: 30944313; PubMed Central PMCID: PMC6447622.

21. Kanehisa M, Sato Y, Kawashima M, Furumichi M, Tanabe M. KEGG as a reference

resource for gene and protein annotation. Nucleic Acids Res. 2016 Jan 4;44(D1):D457-462. doi:10.1093/nar/gkv1070 PubMed PMID: 26476454; PubMed Central PMCID: PMC4702792.

22. Kanehisa M, Goto S. KEGG: kyoto encyclopedia of genes and genomes. Nucleic Acids Res. 2000 Jan 1;28(1):27–30. doi:10.1093/nar/28.1.27 PubMed PMID: 10592173; PubMed Central PMCID: PMC102409.

23. Song YS, Dai MZ, Zhu CX, Huang YF, Liu J, Zhang CD, et al. Validation, Optimization, and Application of the Zebrafish Developmental Toxicity Assay for Pharmaceuticals Under the ICH S5(R3) Guideline. Front Cell Dev Biol. 2021;9:721130. doi:10.3389/fcell.2021.721130 PubMed PMID: 34595173; PubMed Central PMCID: PMC8476914.

24. Off J EU. Directive 2010/63/EU of the European parliament and of the council of 22 September 2010 on the protection of animals used for scientific purposes. OJ L, 2024/1262. 2010. p. 33–79.

25. Qi L, Wang J, Hou S, Liu S, Zhang Q, Zhu S, et al. Unraveling the tumor microenvironment of esophageal squamous cell carcinoma through single-cell sequencing: A comprehensive review. Biochim Biophys Acta BBA - Rev Cancer. 2025 Feb;1880(1):189264. doi:10.1016/j.bbcan.2025.189264

26. Ribatti D, Tamma R, Annese T. Epithelial-Mesenchymal Transition in Cancer: A Historical Overview. Transl Oncol. 2020 Jun;13(6):100773. doi:10.1016/j.tranon.2020.100773

27. Jørgensen CLT, Forsare C, Bendahl PO, Falck AK, Fernö M, Lövgren K, et al. Expression of epithelial-mesenchymal transition-related markers and phenotypes during breast cancer progression. Breast Cancer Res Treat. 2020 Jun;181(2):369–81. doi:10.1007/s10549-020-05627-0

28. Chaudhary R, Goodman LS, Wang S, Asimakopoulos A, Weiskirchen R, Dooley S, et al. Cholesterol modulates type I/II TGF-β receptor complexes and alters the balance between Smad and Akt signaling in hepatocytes. Commun Biol. 2024 Jan 2;7(1):8. doi:10.1038/s42003-023-05654-9

29. Wang Z, Castro N, Bernstein AM, Wolosin JM. TGFβ1-driven SMAD2/3 phosphorylation and myofibroblast emergence are fully dependent on the TGFβ1 pre-activation of MAPKs and controlled by maternal leucine zipper kinase. Cell Signal. 2024 Jan;113:110963. doi:10.1016/j.cellsig.2023.110963

30. Melzer M, Niebert S, Heimann M, Ullm F, Pompe T, Scheiner-Bobis G, et al. Differential Smad2/3 linker phosphorylation is a crosstalk mechanism of Rho/ROCK and canonical TGF-β3 signaling in tenogenic differentiation. Sci Rep. 2024 May 6;14(1):10393. doi:10.1038/s41598-024-60717-z

31. Chia ZJ, Cao Y nan, Little PJ, Kamato D. Transforming growth factor-β receptors: versatile mechanisms of ligand activation. Acta Pharmacol Sin. 2024 Jul;45(7):1337–48. doi:10.1038/s41401-024-01235-6

32. Hu Z, Sui Q, Jin X, Shan G, Huang Y, Yi Y, et al. IL6-STAT3-C/EBPβ-IL6 positive feedback loop in tumor-associated macrophages promotes the EMT and metastasis of lung adenocarcinoma. J Exp Clin Cancer Res. 2024 Feb 29;43(1):63. doi:10.1186/s13046-024-02989-x

33. Sumitomo R, Menju T, Shimazu Y, Toyazaki T, Chiba N, Miyamoto H, et al. M2-like tumor-associated macrophages promote epithelial–mesenchymal transition through the transforming growth factor β/Smad/zinc finger e-box binding homeobox pathway with increased metastatic potential and tumor cell proliferation in lung squamous cell carcinoma. Cancer Sci. 2023 Dec;114(12):4521–34. doi:10.1111/cas.15987

34. Xu J, Ding L, Mei J, Hu Y, Kong X, Dai S, et al. Dual roles and therapeutic targeting of tumor-associated macrophages in tumor microenvironments. Signal Transduct Target Ther. 2025 Aug 25;10(1):268. doi:10.1038/s41392-025-02325-5

35. Kim SW, Kim CW, Moon YA, Kim HS. Reprogramming of tumor-associated macrophages by metabolites generated from tumor microenvironment. Anim Cells Syst. 2024 Dec 31;28(1):123–36. doi:10.1080/19768354.2024.2336249

36. Dalpati N, Rai SK, Sharma P, Sarangi PP. Integrins and integrin-driven secretory pathways as multi-dimensional regulators of tumor-associated macrophage recruitment and reprogramming in tumor microenvironment. Matrix Biol. 2025 Feb;135:55–69. doi:10.1016/j.matbio.2024.12.003

37. Jomova K, Alomar SY, Valko R, Fresser L, Nepovimova E, Kuca K, et al. Interplay of oxidative stress and antioxidant mechanisms in cancer development and progression. Arch Toxicol. 2026 Jan;100(1):27–73. doi:10.1007/s00204-025-04146-5 PubMed PMID: 40906205; PubMed Central PMCID: PMC12858508.

38. He Y, Peng E, Ba X, Wu J, Deng W, Huang Q, et al. ROS Responsive Cerium Oxide Biomimetic Nanoparticles Alleviates Calcium Oxalate Crystals Induced Kidney Injury via Suppressing Oxidative Stress and M1 Macrophage Polarization. Small. 2025 Jan;21(3):e2405417. doi:10.1002/smll.202405417 PubMed PMID: 39629501.

39. Zhao Y, Shen M, Wu L, Yang H, Yao Y, Yang Q, et al. Stromal cells in the tumor microenvironment: accomplices of tumor progression? Cell Death Dis. 2023 Sep 4;14(9):587. doi:10.1038/s41419-023-06110-6 PubMed PMID: 37666813; PubMed Central PMCID: PMC10477351.

40. Pérez-González A, Bévant K, Blanpain C. Cancer cell plasticity during tumor progression, metastasis and response to therapy. Nat Cancer. 2023 Aug;4(8):1063–

82. doi:10.1038/s43018-023-00595-y PubMed PMID: 37537300; PubMed Central PMCID: PMC7615147.

41. Yuan Z, Li Y, Zhang S, Wang X, Dou H, Yu X, et al. Extracellular matrix remodeling in tumor progression and immune escape: from mechanisms to treatments. Mol Cancer. 2023 Mar 11;22(1):48. doi:10.1186/s12943-023-01744-8 PubMed PMID: 36906534; PubMed Central PMCID: PMC10007858.

42. Liu Z, Wang Y, Li L, Liu L, Li Y, Li Z, et al. SNAI2, a potential crossing point between cancer and cardiovascular disease. FASEB J Off Publ Fed Am Soc Exp Biol. 2025 Mar 15;39(5):e70459. doi:10.1096/fj.202500198R PubMed PMID: 40059450.

43. Jiao H, Zhang M, Chen L, Zhang Z. Traditional Chinese Medicine targeting the TGF-β/Smad signaling pathway as a potential therapeutic strategy for renal fibrosis. Front Pharmacol. 2025;16:1513329. doi:10.3389/fphar.2025.1513329 PubMed PMID: 40463902; PubMed Central PMCID: PMC12130906.

44. Chen YX, Jiang XX, Zhang QY, Xu CQ, Hu YM, Jin CY, et al. [Role of TGF-β/Smad signaling pathway in diabetic kidney disease and research progress of traditional Chinese medicine intervention]. Zhongguo Zhong Yao Za Zhi Zhongguo Zhongyao Zazhi China J Chin Mater Medica. 2023 May;48(10):2630–8. doi:10.19540/j.cnki.cjcmm.20221114.401 PubMed PMID: 37282924.

45. Li C, Meng X, Wang L, Dai X. Mechanism of action of non-coding RNAs and traditional Chinese medicine in myocardial fibrosis: Focus on the TGF-β/Smad signaling pathway. Front Pharmacol. 2023;14:1092148. doi:10.3389/fphar.2023.1092148 PubMed PMID: 36843918; PubMed Central PMCID: PMC9947662.

46. Ye H, Duan M. FOXN2 is downregulated in breast cancer and regulates migration, invasion, and epithelial–mesenchymal transition through regulation of SLUG. Cancer Manag Res. 2019 Jan;Volume 11:525–35. doi:10.2147/CMAR.S176938

47. Kim R, Suh Y, Yoo K, Cui Y, Hwang E, Kim H, et al. Phloroglucinol suppresses metastatic ability of breast cancer cells by inhibition of epithelial-mesenchymal cell transition. Cancer Sci. 2015 Jan;106(1):94–101. doi:10.1111/cas.12562

48. Basak U, Sarkar T, Mukherjee S, Chakraborty S, Dutta A, Dutta S, et al. Tumor-associated macrophages: an effective player of the tumor microenvironment. Front Immunol. 2023 Nov 16;14:1295257. doi:10.3389/fimmu.2023.1295257

49. Liao L, Wang YX, Fan SS, Hu YY, Wang XC, Zhang X. The role and clinical significance of tumor-associated macrophages in the epithelial-mesenchymal transition of lung cancer. Front Oncol. 2025;15:1571583. doi:10.3389/fonc.2025.1571583 PubMed PMID: 40304000; PubMed Central PMCID: PMC12037373.

50. Song W, Mazzieri R, Yang T, Gobe GC. Translational Significance for Tumor Metastasis of Tumor-Associated Macrophages and Epithelial–Mesenchymal Transition. Front Immunol. 2017 Sep 13;8:1106. doi:10.3389/fimmu.2017.01106

51. Tang X, Zhu M, Zhu Z, Tang W, Zhang H, Chen Y, et al. Ginsenoside Re inhibits non-small cell lung cancer progression by suppressing macrophage M2 polarization induced by AMPKA1 / STING positive feedback loop. Phytother Res. 2024 Nov;38(11):5088–106. doi:10.1002/ptr.8309

52. Zhao Y, Ni Q, Zhang W, Yu S. Progress in reeducating tumor-associated macrophages in tumor microenvironment. Discov Oncol. 2024 Jul 26;15(1):312. doi:10.1007/s12672-024-01186-8

53. Sun Y, Lian Y, Mei X, Xia J, Feng L, Gao J, et al. Cinobufagin inhibits M2-like tumor-associated macrophage polarization to attenuate the invasion and migration of lung cancer cells. Int J Oncol. 2024 Sep 11;65(5):102. doi:10.3892/ijo.2024.5690

54. Shen L, Li Y, Hu G, Song X, Wang X, Li X, et al. Astragaloside IV suppresses the migration and EMT progression of cervical cancer cells by inhibiting macrophage M2 polarization through TGFβ/Smad2/3 signaling. Funct Integr Genomics. 2023 Apr 21;23(2):133. doi:10.1007/s10142-023-01017-z PubMed PMID: 37081108.

55. Deng XX, Jiao YN, Hao HF, Xue D, Bai CC, Han SY. Taraxacum mongolicum extract inhibited malignant phenotype of triple-negative breast cancer cells in tumor-associated macrophages microenvironment through suppressing IL-10 / STAT3 / PD-L1 signaling pathways. J Ethnopharmacol. 2021 Jun 28;274:113978. doi:10.1016/j.jep.2021.113978 PubMed PMID: 33716082.

56. Aggarwal V, Tuli HS, Varol A, Thakral F, Yerer MB, Sak K, et al. Role of Reactive Oxygen Species in Cancer Progression: Molecular Mechanisms and Recent Advancements. Biomolecules. 2019 Nov 13;9(11):735. doi:10.3390/biom9110735 PubMed PMID: 31766246; PubMed Central PMCID: PMC6920770.

57. Jiang J, Wang K, Chen Y, Chen H, Nice EC, Huang C. Redox regulation in tumor cell epithelial-mesenchymal transition: molecular basis and therapeutic strategy. Signal Transduct Target Ther. 2017;2:17036. doi:10.1038/sigtrans.2017.36 PubMed PMID: 29263924; PubMed Central PMCID: PMC5661624.

58. Griess B, Mir S, Datta K, Teoh-Fitzgerald M. Scavenging reactive oxygen species selectively inhibits M2 macrophage polarization and their pro-tumorigenic function in part, via Stat3 suppression. Free Radic Biol Med. 2020 Feb 1;147:48–60. doi:10.1016/j.freeradbiomed.2019.12.018 PubMed PMID: 31863907; PubMed Central PMCID: PMC10035558.

59. Zhang Y, Choksi S, Chen K, Pobezinskaya Y, Linnoila I, Liu ZG. ROS play a critical role in the differentiation of alternatively activated macrophages and the occurrence of

tumor-associated macrophages. Cell Res. 2013 Jul;23(7):898–914. doi:10.1038/cr.2013.75 PubMed PMID: 23752925; PubMed Central PMCID: PMC3698641.

60. Chang D, Yang J, Li Y, Min S, Ma Y, Xu T, et al. Spatiotemporally Controlled Nanomicelles for Synergistic Phototherapy and Immune Reprogramming in Triple-Negative Breast Cancer. ACS Nano. 2025 Oct 21;19(41):36323–41. doi:10.1021/acsnano.5c09413 PubMed PMID: 41071998.

61. Mo W, Liu S, Zhao X, Wei F, Li Y, Sheng X, et al. ROS Scavenging Nanozyme Modulates Immunosuppression for Sensitized Cancer Immunotherapy. Adv Healthc Mater. 2023 Aug;12(21):e2300191. doi:10.1002/adhm.202300191 PubMed PMID: 37031357.

62. Su X, Yan X, Zhang H. The tumor microenvironment in hepatocellular carcinoma: mechanistic insights and therapeutic potential of traditional Chinese medicine. Mol Cancer. 2025 Jun 10;24(1):173. doi:10.1186/s12943-025-02378-8 PubMed PMID: 40495147; PubMed Central PMCID: PMC12150456.

63. Huang YC, Huang SJ, Yang HY, Tsai CY, Chang HC, Chi HC, et al. Development of a compound herbal formulation (HBK) with antitumor and antioxidant functions for cancer adjuvant therapy. Phytomedicine Int J Phytother Phytopharm. 2025 Nov;147:157212. doi:10.1016/j.phymed.2025.157212 PubMed PMID: 40934759.

64. Zhang X, Gao H, Wei D, Pei X, Zhang Y, Wang J, et al. ROS Responsive Nanoparticles Encapsulated with Natural Medicine Remodel Autophagy Homeostasis in Breast Cancer. ACS Appl Mater Interfaces. 2023 Jun 28;15(25):29827–40. doi:10.1021/acsami.3c03068 PubMed PMID: 37314154.

65. Luo Y, Yin S, Lu J, Zhou S, Shao Y, Bao X, et al. Tumor microenvironment: a prospective target of natural alkaloids for cancer treatment. Cancer Cell Int. 2021 Jul 20;21(1):386. doi:10.1186/s12935-021-02085-6 PubMed PMID: 34284780; PubMed Central PMCID: PMC8290600.

66. Zhang Y, Lou Y, Wang J, Yu C, Shen W. Research Status and Molecular Mechanism of the Traditional Chinese Medicine and Antitumor Therapy Combined Strategy Based on Tumor Microenvironment. Front Immunol. 2020;11:609705. doi:10.3389/fimmu.2020.609705 PubMed PMID: 33552068; PubMed Central PMCID: PMC7859437.

Figure Legend

Figure 1. Phloroglucinol (PhG) suppresses the migration and invasion of esophageal cancer cells in vitro independent of cytotoxicity.

(A) Schematic illustration of Phloroglucinol (PhG) derived from brown algae and its chemical structure (1,3,5-trihydroxybenzene). **(B, C)** Cell viability of human ESCC

cells (KYSE150) and mouse esophageal cancer cells (AKR) treated with the indicated concentrations of PhG (0–100 μg/mL) for 24 h and 48 h, assessed by the CCK-8 assay. **(D, E)** Representative light microscopy images of wound-healing assays demonstrating the lateral migration of KYSE150 (D) and AKR (E) cells treated with various concentrations of PhG at the indicated time points. **(F, G)** Quantitative analysis of the scratch healing rate (%) for KYSE150 (F) and AKR (G) cells. (H, I) Representative images and corresponding quantification of Transwell migration and Matrigel invasion assays for KYSE150 (H) and AKR (I) cells following treatment with vehicle (0 μg/mL) or 50 μg/mL PhG. All data are presented as the mean ±SD from three independent experiments.

Figure 2. PhG Inhibits Metastasis of ESCC Cells *in vivo*

(A–E) Assessment of the in vivo safety profile of PhG in zebrafish larvae. Healthy zebrafish larvae at 48 hpf were exposed to PhG (0, 25, or 50 μg/mL) for 48 h. (A) Representative bright-field images showing larval morphology. (B) Quantification of larval body length. (C) Survival rates of zebrafish larvae. (D) Heart rate of zebrafish larvae. (E) Touch-evoked escape response of zebrafish larvae. (F–G) Evaluation of the anti-metastatic effect of PhG in a zebrafish xenograft model. DiI-labeled KYSE150 cells were injected into the perivitelline space of 48-hpf zebrafish larvae, followed by treatment with PhG. (F) Representative fluorescence images showing tumor cell dissemination at 48, 72, and 96 hpf. (G) Quantification of metastatic dissemination at 72 and 96 hpf. (H–J) Evaluation of the anti-metastatic effect of PhG in a mouse footpad tumor model using murine ESCC AKR cells. (H) Images showing the metastatic status of the popliteal and inguinal lymph nodes in individual mice, with metastatic lesions indicated by red arrows. (I) Quantification of metastatic lymph nodes. (J) Representative H&E-stained sections showing metastatic lesions in the regional lymph nodes. Data are presented as the mean ± SD; ns, not significant.

Figure 3. Transcriptome profiling identifies SNAI2 and implicates TGF-β signaling in PhG-mediated EMT regulation

(A) Bar graph summarizing the number of differentially expressed genes (DEGs), including upregulated (red) and downregulated (blue) transcripts, in KYSE150 cells treated with 50 μg/mL PhG for 24 h compared to the control (cutoff criteria: $|\log_2 FC| > 1$ and FDR < 0.05). **(B)** Venn diagram illustrating the intersection between the identified DEGs and the Hallmark EMT gene set (MSigDB), yielding 26 PhG-responsive EMT-associated genes. **(C)** Circular heatmap depicting the hierarchical clustering and expression profiles of the 26 overlapping EMT-related genes. The marked downregulation of the key transcription factor SNAI2 is prominently highlighted. **(D)** RT-qPCR validation of SNAI2 mRNA expression levels in KYSE150 cells following PhG treatment. Data are presented as the mean ± SD of three independent experiments. **(E)** Co-expression network analysis mapping the 121 DEGs

that are highly correlated with SNAI2 expression ($|R| > 0.9$ and $|\log_2FC| > 1.5$). **(F)** Transcriptional regulatory analysis indicating the significant enrichment of MYC-associated target genes within the SNAI2 co-expressed gene set. **(G)** Functional and pathway enrichment analysis of the 121 SNAI2-correlated genes. Abbreviations: PhG50, 50 μg/mL PhG; DEGs, differentially expressed genes; EMTs, epithelial-mesenchymal transition genes.

Figure 4. Phloroglucinol abrogates TGF-β-driven EMT in ESCC cells by intercepting the SMAD2/3/SNAI2 signaling axis

(A–E) Representative Western blot images **(A)** and relative densitometric quantification **(B–E)** of E-cadherin, N-cadherin, Vimentin, and Slug in KYSE150 cells treated with the indicated concentrations of PhG (0, 25, and 50 μg/mL) for 24 h. **(F–L)** Representative Western blot images **(F)** and corresponding quantification **(G–L)** of SMAD2/3 phosphorylation and EMT-related proteins in KYSE150 cells. For analysis of SMAD2/3 phosphorylation, cells were pretreated with PhG for 1 h followed by stimulation with recombinant human TGF-β (rhTGF-β) for 30 min. For EMT marker analysis, cells were co-treated with PhG and rhTGF-β for 24 h. (M–S) Representative Western blot images **(M)** and corresponding quantification **(N–S)** in the murine AKR cell line, confirming the inhibitory effect of PhG on TGF-β/SMAD signaling and EMT. **(T–W)** Representative images and quantitative analysis of wound-healing assays showing the inhibitory effect of PhG on rhTGF-β-enhanced cell migration in KYSE150 **(T, U)** and AKR **(V, W)** cells after 24 h of co-treatment. Target protein levels were normalized to β-actin, and phosphorylated SMAD2/3 (p-SMAD2/3) was normalized to total SMAD2/3. Data are presented as mean ± SD from three independent experiments.

Figure 5. Molecular docking suggests a potential interaction between PhG and TGFBR1

(A) Left: overall 3D conformation of SB431542 docked into the ATP-binding pocket of TGFBR1 (PDB: 1VJY), with the binding site highlighted by a red box. Middle: detailed 3D view of the interaction interface, showing SB431542 (green sticks) and key residues. Right: 2D schematic diagram of the interactions between SB431542 and the active-site residues of TGFBR1. **(B–D)** Similar docking analyses for PhG (red sticks) with TGFBR1 (B), SMAD2 (C), and SMAD3 (D).

Figure 6. Phloroglucinol attenuates macrophage-mediated ESCC cell migration by reducing TAM-derived TGF-β secretion

(A) Schematic workflow illustrating TAM induction with ESCC-conditioned medium (EC-CM) in the presence or absence of PhG and subsequent collection of M0-CM, TAM-CM, and TAM(PhG)-CM. **(B, C)** Effects of PhG treatment (up to 100 μg/mL) for 48 h on the viability of THP-1-derived macrophages (B) and RAW264.7 cells (C), as determined by CCK-8 assay. **(D)** Representative morphological images and corresponding flow cytometric analysis of THP-1-derived macrophages stimulated

with ESCC-conditioned medium in the presence or absence of PhG. **(E)** Quantitative analysis of the percentage of CD163- and CD86-positive cells, representative fluorescence histograms, and median fluorescence intensity (MFI) in THP-1-derived macrophages under the indicated treatment conditions. **(F)** Representative morphological images and corresponding flow cytometric analysis of RAW264.7 cells stimulated with ESCC-conditioned medium in the presence or absence of PhG. **(G)** Quantitative analysis of the percentage of CD206- and CD86-positive cells, representative fluorescence histograms, and median fluorescence intensity (MFI) in RAW264.7 cells under the indicated treatment conditions. **(H, L)** ELISA quantification of secreted TGF-β levels in CM derived from different macrophage groups in the human THP-1 (H) and murine RAW264.7 (L) models. **(I, M)** CCK-8 assays evaluating the effects of SB431542 treatment (up to 20 μM) for 24 h on the viability of KYSE150 (I) and AKR (M) cells. **(J, K)** Representative wound-healing images and quantitative analysis of wound closure evaluating the effects of the indicated CM (M0-CM, TAM-CM, and TAM(PhG-CM), with or without SB431542 (2.5 μM), on KYSE150 cell migration after 24 h. **(N, O)** Corresponding wound-healing images and quantitative analysis using the murine RAW264.7 macrophage–AKR cell model. All data are presented as the mean ± SD from three independent experiments.

Figure 7. Phloroglucinol attenuates intracellular ROS accumulation in ESCC cells and macrophages.

(A, C) Representative flow cytometric histograms of intracellular ROS levels in KYSE150 (A) and AKR (C) cells following TGF-β stimulation in the absence or presence of PhG. **(B, D)** Quantification of intracellular ROS fluorescence intensity in KYSE150 (B) and AKR (D) cells. **(E, G)** Representative flow cytometric histograms of intracellular ROS levels in THP-1-derived (E) and RAW264.7 (G) macrophages following stimulation with ESCC-conditioned medium in the absence or presence of PhG. **(F, H)** Quantification of intracellular ROS fluorescence intensity in THP-1-derived (F) and RAW264.7 (H) macrophages. All data are presented as the mean ± SD from three independent experiments.

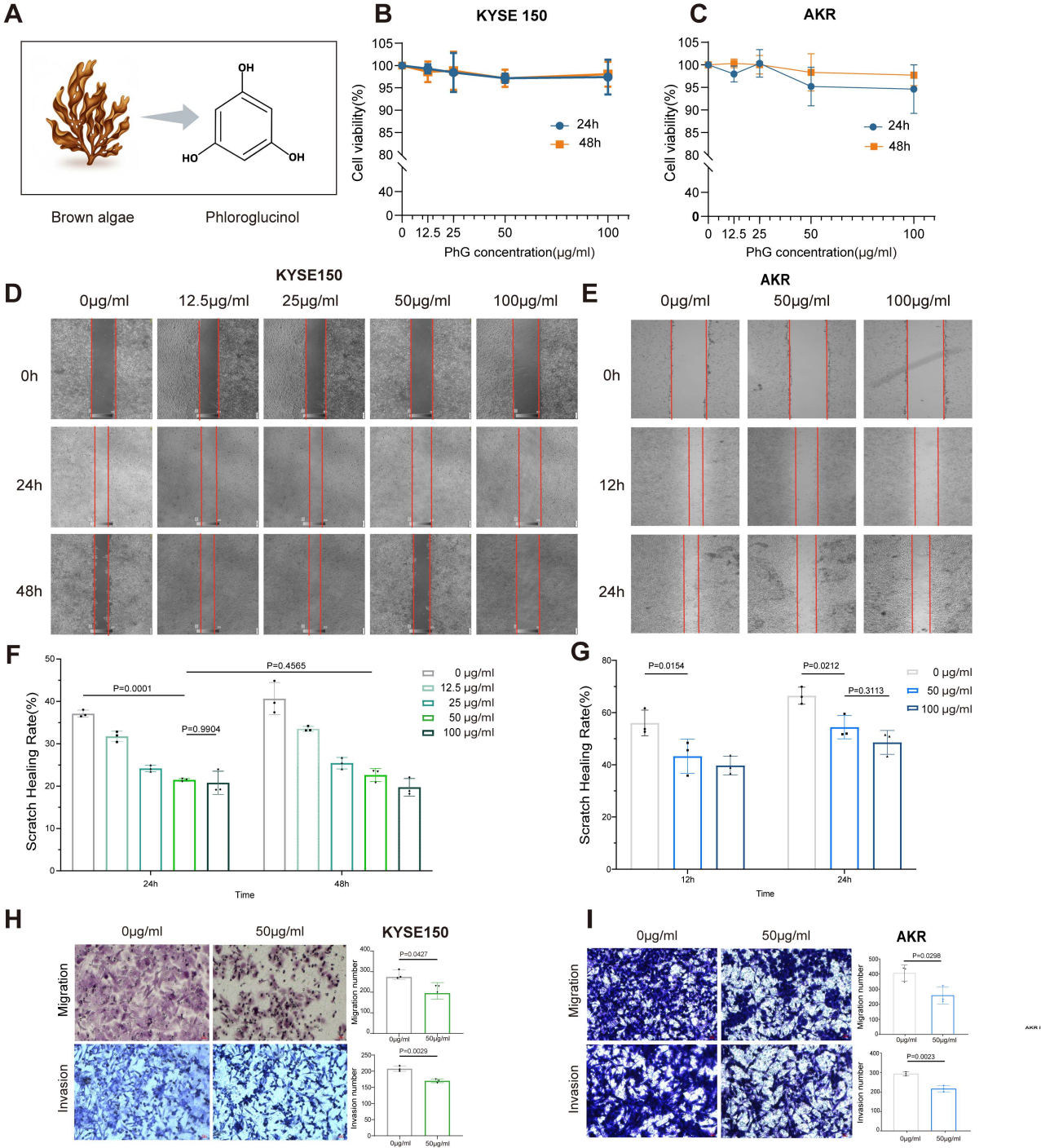
Graphical abstract. Phloroglucinol suppresses ESCC metastasis through coordinated inhibition of tumor cell-intrinsic and TAM-derived TGF-β signaling

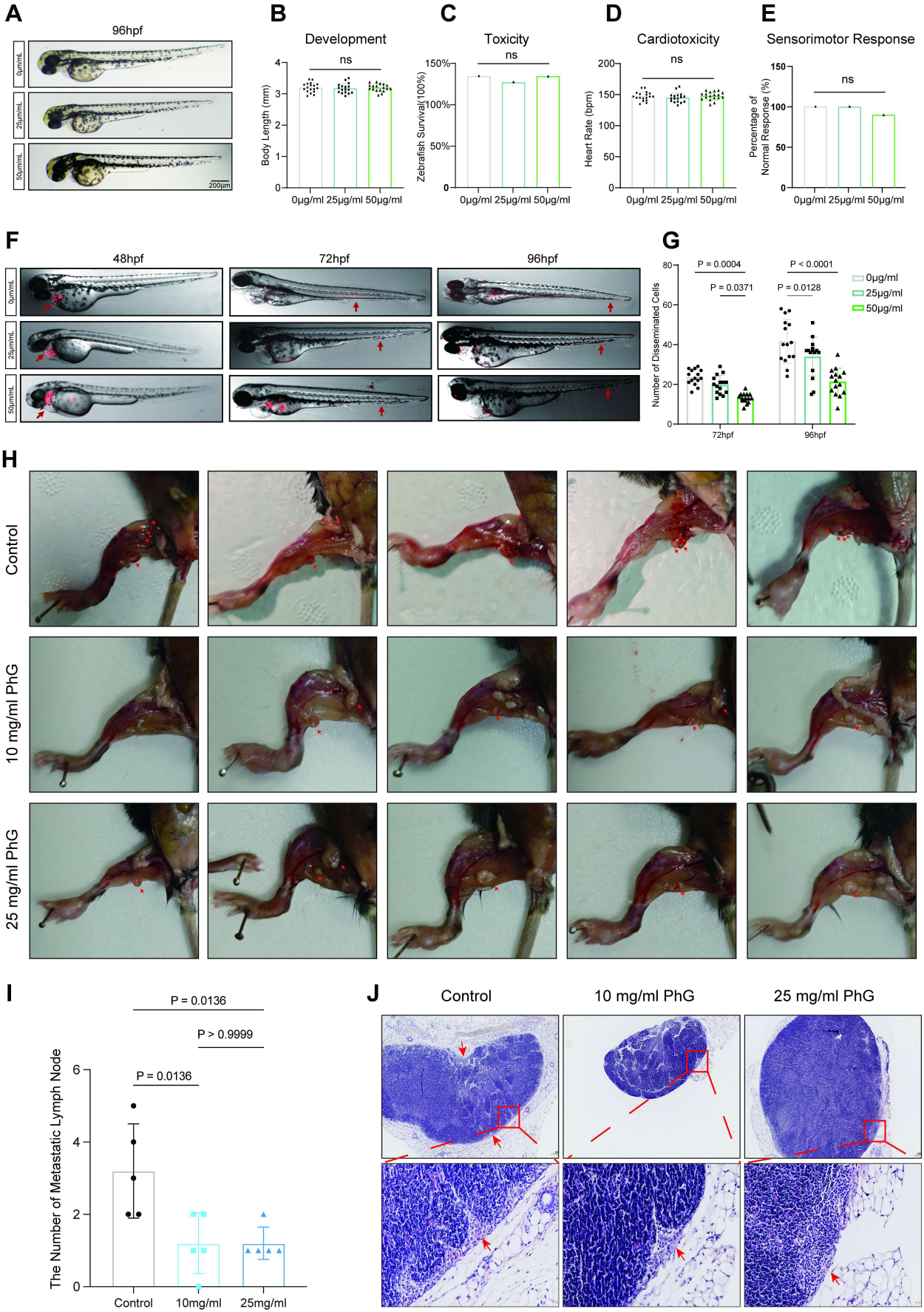
Phloroglucinol suppresses ESCC metastasis through two complementary mechanisms. In ESCC cells, PhG attenuates TGF-β-induced SMAD2/3 phosphorylation and inhibits the downstream SNAI2/Slug-associated EMT program, thereby reducing migratory and metastatic phenotypes. In the tumor microenvironment, PhG modulates tumor-conditioned macrophage phenotypes and reduces TAM-derived TGF-β secretion, consequently weakening paracrine TGF-β signaling and TAM-mediated ESCC cell migration. ESCC: Esophageal squamous cell carcinoma, TAM: ESCC-

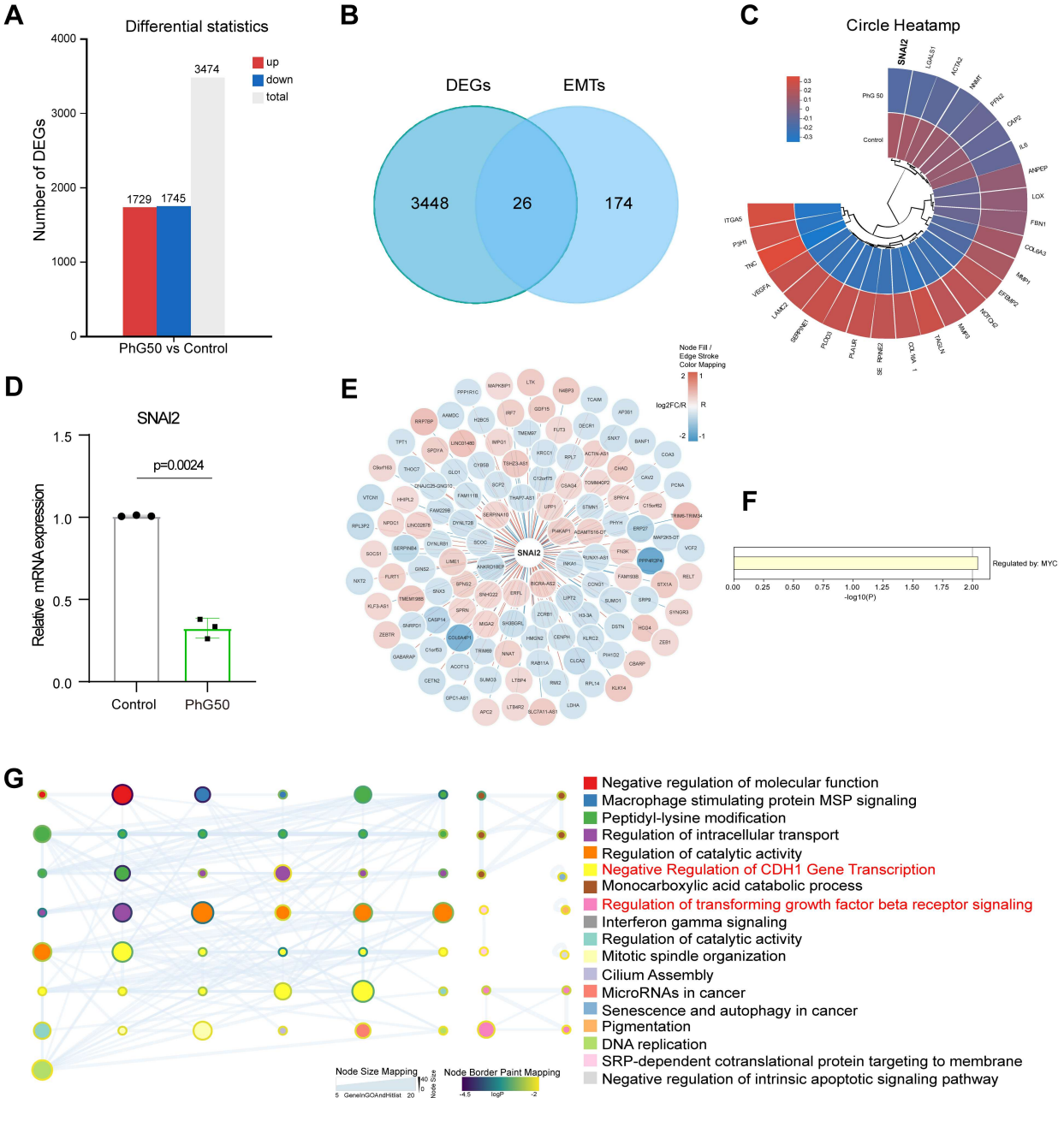
conditioned macrophages, TAM + PhG: PhG-treated ESCC-conditioned macrophages.

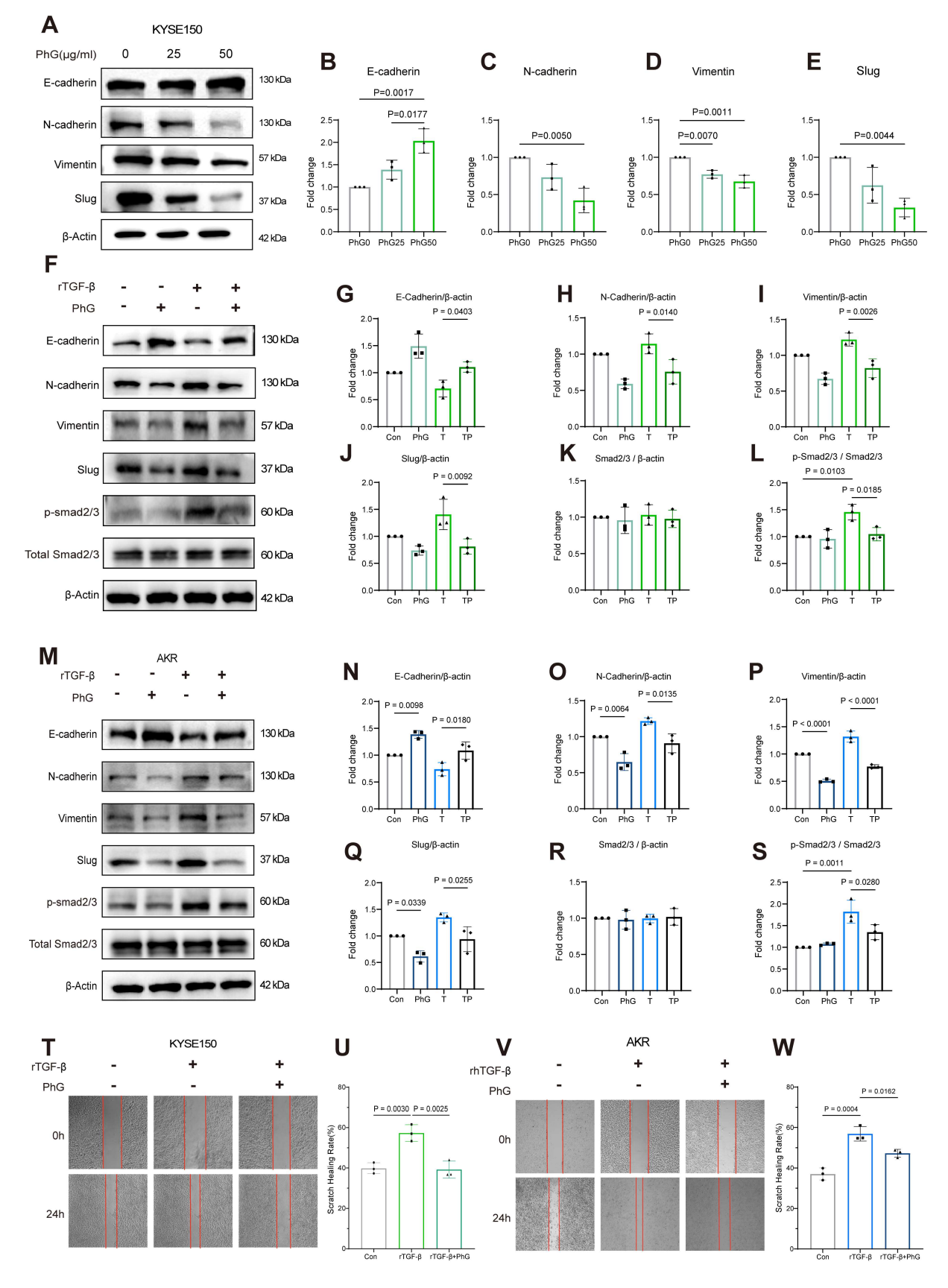
Table 1. Molecular docking results of PhG and SB431542 with TGF-β signaling components.

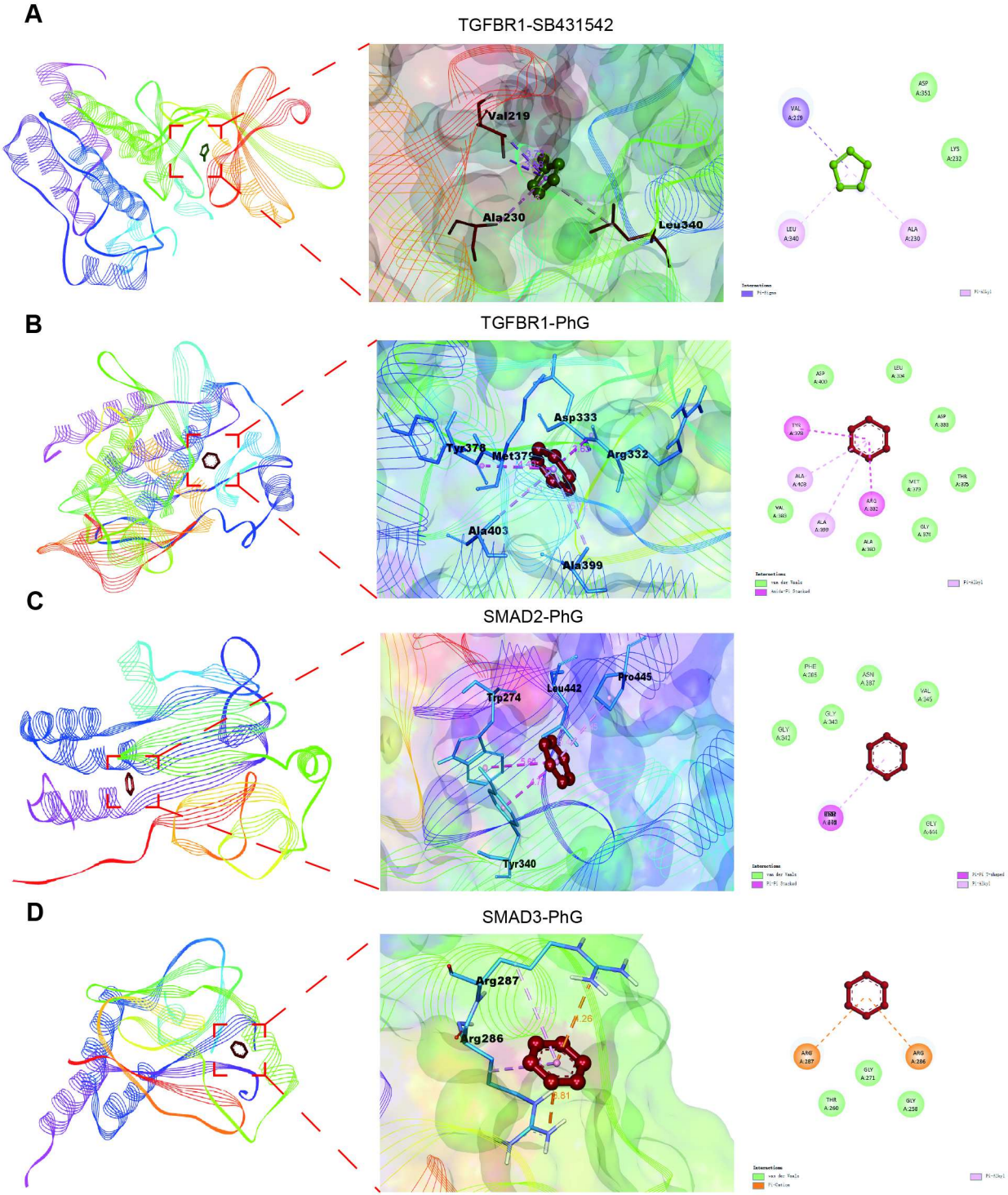
Target Protein	PDB ID	Ligand	Binding Energy ΔG (kcal/mol)	Key Interacting Residues	Main Interaction Types
TGFBR1 (Control)	1VJY	SB431542	−10.97	Lys232, Asp351, Val219, Leu340, Ala230	Pi-Sigma, Pi-Alkyl
TGFBR1	1VJY	PhG	−6.093	Tyr378, Ala403, Ala399, Arg332, Asp400, Leu334, Asp333, Thr375, Met379, Gly374, Ala380, Val383	van der Waals, Pi-Alkyl, Amide-Pi stacked
SMAD2	1KHX	PhG	−4.964	Phe385, Asn387, Val345, Gly343, Gly342, Gly444, Tyr340, Typ274	van der Waals, Pi-Pi T-shaped, Pi-Pi stacked, Pi-Alkyl
SMAD3	1MJS	PhG	−4.225	Gly271, Thr260, Gly258, Arg287, Arg286	van der Waals, Pi-Alkyl, Pi-Cation

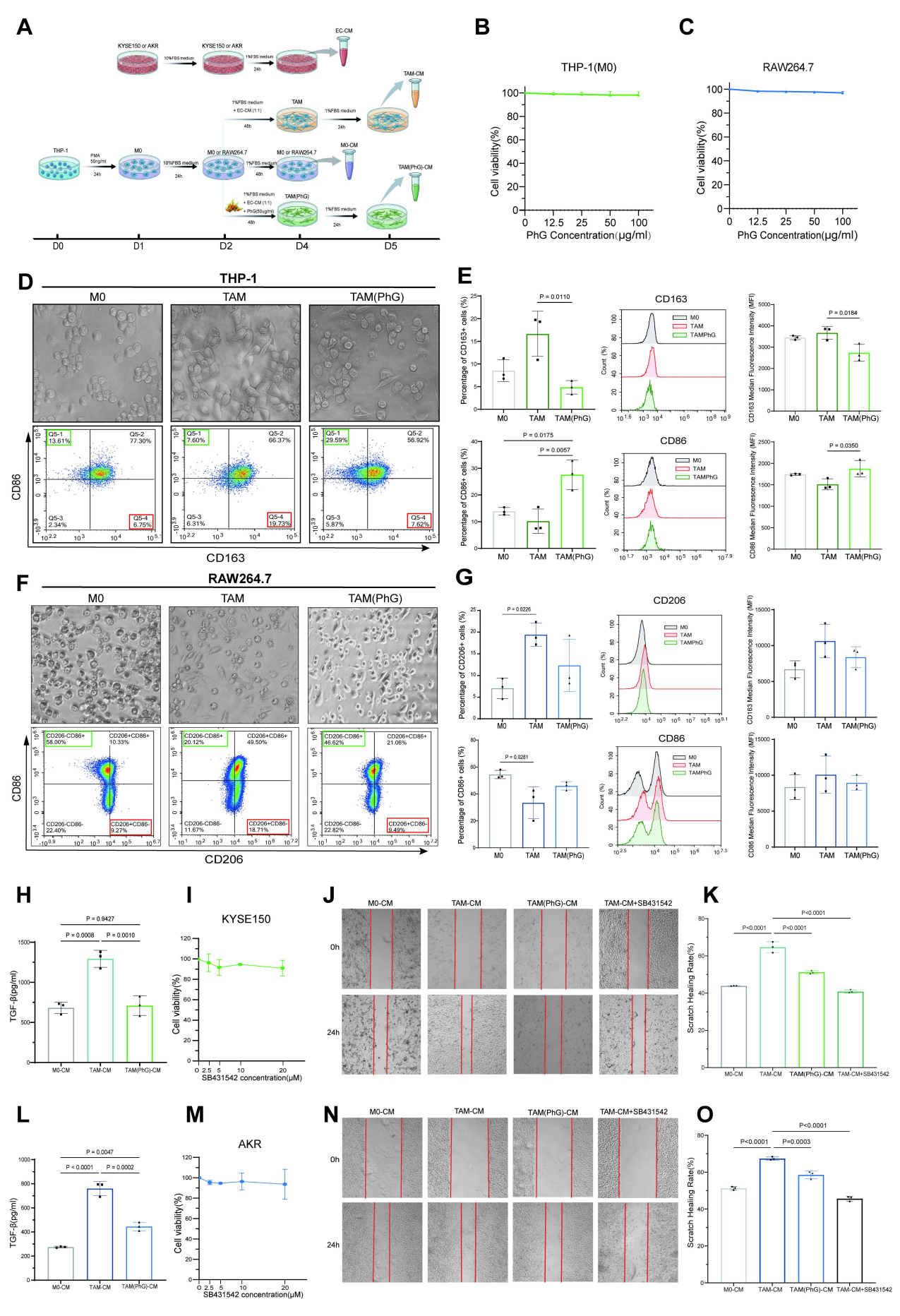

A
OH
HO
OH
Brown algae
Phloroglucinol
B
KYSE 150
Cell viability(%)
24h
48h
PhG concentration(μg/ml)
C
AKR
Cell viability(%)
24h
48h
PhG concentration(μg/ml)
D
KYSE150
0μg/ml
12.5μg/ml
25μg/ml
50μg/ml
100μg/ml
0h
24h
48h
E
AKR
0μg/ml
50μg/ml
100μg/ml
0h
12h
24h
F
Scratch Healing Rate(%)
P=0.0001
P=0.9904
P=0.4565
0 μg/ml
12.5 μg/ml
25 μg/ml
50 μg/ml
100 μg/ml
24h
48h
Time
G
Scratch Healing Rate(%)
P=0.0154
P=0.0212
P=0.3113
0 μg/ml
50 μg/ml
100 μg/ml
12h
24h
Time
H
0μg/ml
50μg/ml
KYSE150
Migration
Invasion
P=0.0427
Migration number
P=0.0029
Invasion number
0μg/ml
50μg/ml
I
0μg/ml
50μg/ml
AKR
Migration
Invasion
P=0.0298
Migration number
P=0.0023
Invasion number
0μg/ml
50μg/ml

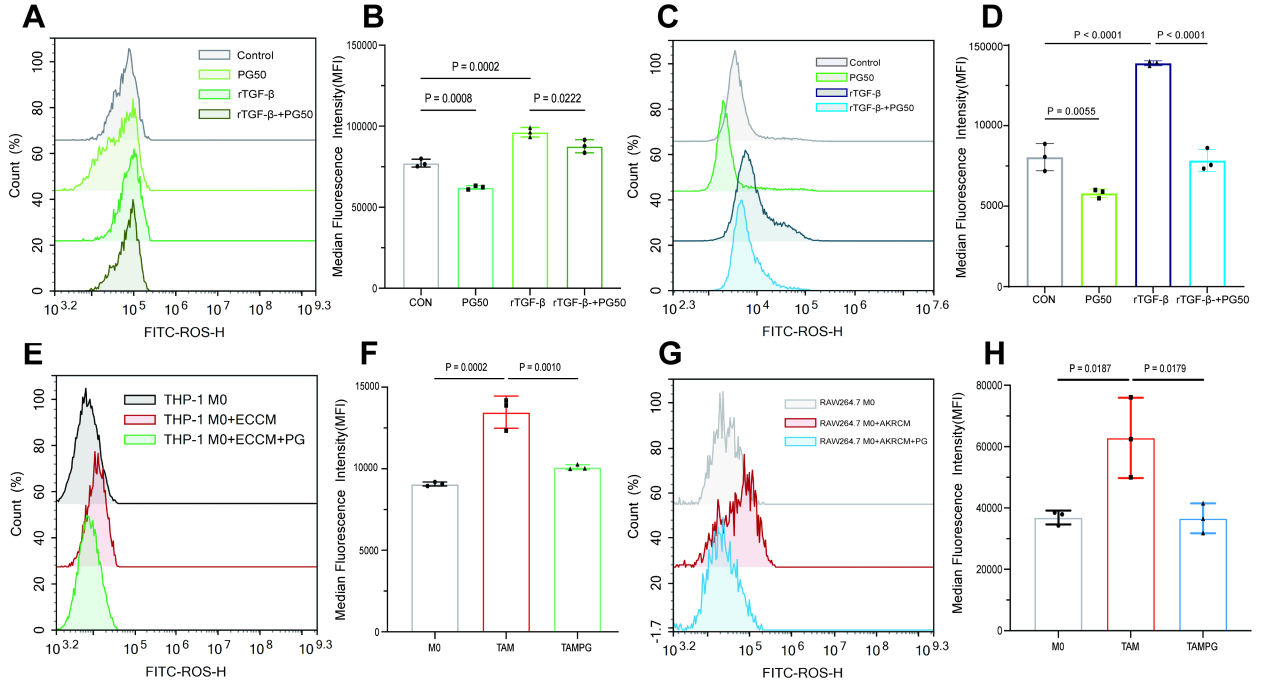

A
96hpf
0μm/mL
25μm/mL
50μm/mL
200μm
B
Development
ns
Body Length (mm)
0μg/ml 25μg/ml 50μg/ml
C
Toxicity
ns
Zebrafish Survival(100%)
150%
100%
50%
0
0μg/ml 25μg/ml 50μg/ml
D
Cardiotoxicity
ns
Heart Rate (bpm)
0μg/ml 25μg/ml 50μg/ml
E
Sensorimotor Response
ns
Percentage of Normal Response (%)
0μg/ml 25μg/ml 50μg/ml
F
48hpf
72hpf
96hpf
0μm/mL
25μm/mL
50μm/mL
G
P = 0.0004
P = 0.0371
P < 0.0001
P = 0.0128
0μg/ml
25μg/ml
50μg/ml
Number of Disseminated Cells
72hpf
96hpf
H
Control
10 mg/ml PhG
25 mg/ml PhG
I
P = 0.0136
P > 0.9999
P = 0.0136
The Number of Metastatic Lymph Node
Control
10mg/ml
25mg/ml
J
Control
10 mg/ml PhG
25 mg/ml PhG


A
Differential statistics
Number of DEGs
4000
3000
2000
1000
0
up
down
total
3474
1729
1745
PhG50 vs Control
B
DEGs
EMTs
3448
26
174
C
Circle Heatamp
SNAI2
PhG 50
Control
ITGA5
P3H1
TNC
VEGFA
LAMC2
SERPINE1
FLOD3
PLAUR
SE
RHNB2
COL18A 1
TAGLN
MMP3
NOTCH2
EFEMP2
MMP1
COL6A3
FBN1
LOX
ANPEP
IL6
CAV2
PTN2
NMMT
ACTN2
LGALS1
D
SNAI2
p=0.0024
Relative mRNA expression
1.5
1.0
0.5
0.0
Control
PhG50
E
Node Fill / Edge Stroke Color Mapping
log2FC/R
SNAI2
F
Regulated by: MYC
-log10(P)
G
Node Size Mapping
Node Border Paint Mapping
Negative regulation of molecular function
Macrophage stimulating protein MSP signaling
Peptidyl-lysine modification
Regulation of intracellular transport
Regulation of catalytic activity
Negative Regulation of CDH1 Gene Transcription
Monocarboxylic acid catabolic process
Regulation of transforming growth factor beta receptor signaling
Interferon gamma signaling
Regulation of catalytic activity
Mitotic spindle organization
Cilium Assembly
MicroRNAs in cancer
Senescence and autophagy in cancer
Pigmentation
DNA replication
SRP-dependent cotranslational protein targeting to membrane
Negative regulation of intrinsic apoptotic signaling pathway


A
KYSE150
PhG(μg/ml) 0 25 50
E-cadherin
N-cadherin
Vimentin
Slug
β-Actin
130 kDa
130 kDa
57 kDa
37 kDa
42 kDa
B
E-cadherin
P=0.0017
P=0.0177
C
N-cadherin
P=0.0050
D
Vimentin
P=0.0011
P=0.0070
E
Slug
P=0.0044
Fold change
PhG0 PhG25 PhG50
F
rTGF-β
PhG
E-cadherin
N-cadherin
Vimentin
Slug
p-smad2/3
Total Smad2/3
β-Actin
130 kDa
130 kDa
57 kDa
37 kDa
60 kDa
60 kDa
42 kDa
G
E-Cadherin/β-actin
P = 0.0403
H
N-Cadherin/β-actin
P = 0.0140
I
Vimentin/β-actin
P = 0.0026
J
Slug/β-actin
P = 0.0092
K
Smad2/3 / β-actin
L
p-Smad2/3 / Smad2/3
P = 0.0103
P = 0.0185
Con PhG T TP
M
AKR
rTGF-β
PhG
E-cadherin
N-cadherin
Vimentin
Slug
p-smad2/3
Total Smad2/3
β-Actin
130 kDa
130 kDa
57 kDa
37 kDa
60 kDa
60 kDa
42 kDa
N
E-Cadherin/β-actin
P = 0.0098
P = 0.0180
O
N-Cadherin/β-actin
P = 0.0064
P = 0.0135
P
Vimentin/β-actin
P < 0.0001
P < 0.0001
Q
Slug/β-actin
P = 0.0339
P = 0.0255
R
Smad2/3 / β-actin
S
p-Smad2/3 / Smad2/3
P = 0.0011
P = 0.0280
Con PhG T TP
T
KYSE150
rTGF-β
PhG
0h
24h
U
P = 0.0030
P = 0.0025
Scratch Healing Rate(%)
Con rTGF-β rTGF-β+PhG
V
AKR
rhTGF-β
PhG
0h
24h
W
P = 0.0004
P = 0.0162
Scratch Healing Rate(%)
Con rTGF-β rTGF-β+PhG


A
TGFBR1-SB431542
Val219
Ala230
Leu340
B
TGFBR1-PhG
Asp333
Tyr378
Met375
Arg332
Ala403
Ala399
C
SMAD2-PhG
Trp274
Leu442
Pro445
Tyr340
D
SMAD3-PhG
Arg287
Arg286


A
KYSE150 or AKR
10%FBS medium
KYSE150 or AKR
1%FBS medium
24h
EC-CM
TAM-CM
1%FBS medium
+ EC-CM (1:1)
48h
TAM
1%FBS medium
24h
THP-1
PMA
50ng/ml
24h
M0
10%FBS medium
24h
M0 or RAW264.7
1%FBS medium
48h
M0 or RAW264.7
M0-CM
TAM(PhG)-CM
1%FBS medium
+ EC-CM (1:1)
+ PhG(50μg/ml)
48h
TAM(PhG)
1%FBS medium
24h
D0
D1
D2
D4
D5
B
THP-1(M0)
Cell viability(%)
PhG Concentration(μg/ml)
C
RAW264.7
Cell viability(%)
PhG Concentration(μg/ml)
D
THP-1
M0
TAM
TAM(PhG)
CD86
CD163
Q5-1 13.61%
Q5-2 77.30%
Q5-3 2.34%
Q5-4 6.75%
Q5-1 7.60%
Q5-2 66.37%
Q5-3 6.31%
Q5-4 19.73%
Q5-1 29.59%
Q5-2 56.92%
Q5-3 5.87%
Q5-4 7.62%
E
Percentage of CD163+ cells (%)
P = 0.0110
CD163
Count (%)
M0
TAM
TAMPhG
CD163 Median Fluorescence Intensity (MFI)
P = 0.0184
Percentage of CD86+ cells (%)
P = 0.0175
P = 0.0057
CD86
CD86 Median Fluorescence Intensity (MFI)
P = 0.0350
F
RAW264.7
M0
TAM
TAM(PhG)
CD86
CD206
CD206-CD86+ 58.00%
CD206+CD86+ 10.33%
CD206-CD86- 22.40%
CD206+CD86- 9.27%
CD206-CD86+ 20.12%
CD206+CD86+ 49.50%
CD206-CD86- 11.67%
CD206+CD86- 18.71%
CD206-CD86+ 46.62%
CD206+CD86+ 21.06%
CD206-CD86- 22.82%
CD206+CD86- 9.49%
G
Percentage of CD206+ cells (%)
P = 0.0226
CD206
Count (%)
M0
TAM
TAMPhG
CD163 Median Fluorescence Intensity (MFI)
Percentage of CD86+ cells (%)
P = 0.0281
CD86
CD86 Median Fluorescence Intensity (MFI)
H
TGF-β(pg/ml)
P = 0.9427
P = 0.0008
P = 0.0010
M0-CM
TAM-CM
TAM(PhG)-CM
I
KYSE150
Cell viability(%)
SB431542 concentration(μM)
J
M0-CM
TAM-CM
TAM(PhG)-CM
TAM-CM+SB431542
0h
24h
K
Scratch Healing Rate(%)
P<0.0001
P<0.0001
P<0.0001
M0-CM
TAM-CM
TAM(PhG)-CM
TAM-CM+SB431542
L
TGF-β(pg/ml)
P = 0.0047
P < 0.0001
P = 0.0002
M0-CM
TAM-CM
TAM(PhG)-CM
M
AKR
Cell viability(%)
SB431542 concentration(μM)
N
M0-CM
TAM-CM
TAM(PhG)-CM
TAM-CM+SB431542
0h
24h
O
Scratch Healing Rate(%)
P<0.0001
P<0.0001
P=0.0003
M0-CM
TAM-CM
TAM(PhG)-CM
TAM-CM+SB431542


A
Control
PG50
rTGF-β
rTGF-β-+PG50
Count (%)
FITC-ROS-H
B
P = 0.0002
P = 0.0008
P = 0.0222
Median Fluorescence Intensity(MFI)
CON
PG50
rTGF-β
rTGF-β-+PG50
C
Control
PG50
rTGF-β
rTGF-β-+PG50
Count (%)
FITC-ROS-H
D
P < 0.0001
P < 0.0001
P = 0.0055
Median Fluorescence Intensity(MFI)
CON
PG50
rTGF-β
rTGF-β-+PG50
E
THP-1 M0
THP-1 M0+ECCM
THP-1 M0+ECCM+PG
Count (%)
FITC-ROS-H
F
P = 0.0002
P = 0.0010
Median Fluorescence Intensity(MFI)
M0
TAM
TAMPG
G
RAW264.7 M0
RAW264.7 M0+AKRCM
RAW264.7 M0+AKRCM+PG
Count (%)
FITC-ROS-H
H
P = 0.0187
P = 0.0179
Median Fluorescence Intensity(MFI)
M0
TAM
TAMPG

Supplementary Files

This is a list of supplementary files associated with this preprint. Click to download.

- KYSE150Fig4F.SupplementaryMaterial.pdf
- KYSE150Fig4ASupplementaryMaterial.pdf
- AKRFig4M.SupplementaryMaterial.pdf
- Graphicalabstract.tif